



Trace Element and Isotope Systematics in Vent Fluids and Sulphides From Maka Volcano, North Eastern Lau Spreading Centre: Insights Into Three-Component Fluid Mixing

Lukas Klose^{1,2,*†}, Manuel Keith^{3,*†}, Daniel Hafermaas³, Charlotte Kleint^{2,4,1}, Wolfgang Bach^{2,4}, Alexander Diehl^{2,4}, Frederike Wilckens^{2,4}, Christian Peters⁵, Harald Strauss⁵, Reiner Klemm³, Robert van Geldern³, Karsten Matthias Haase³ and Andrea Koschinsky^{1,2}

OPEN ACCESS

Edited by:

Zhilei Sun,
Qingdao Institute of Marine Geology
(QIMG), China

Reviewed by:

Hu Wang,
Tongji University, China
Baoju Yang,
Ministry of Natural Resources, China

*Correspondence:

Lukas Klose
lu.klose@jacobs-university.de
Manuel Keith
manuel.keith@fau.de

[†]These Authors have contributed
equally to this work and share first
authorship

Specialty section:

This article was submitted to
Geochemistry,
a section of the journal
Frontiers in Earth Science

Received: 14 September 2021

Accepted: 09 November 2021

Published: 07 December 2021

Citation:

Klose L, Keith M, Hafermaas D,
Kleint C, Bach W, Diehl A, Wilckens F,
Peters C, Strauss H, Klemm R,
van Geldern R, Haase KM and
Koschinsky A (2021) Trace Element
and Isotope Systematics in Vent Fluids
and Sulphides From Maka Volcano,
North Eastern Lau Spreading Centre:
Insights Into Three-Component
Fluid Mixing.
Front. Earth Sci. 9:776925.
doi: 10.3389/feart.2021.776925

¹Department of Physics & Earth Sciences, Jacobs University Bremen, Bremen, Germany, ²Center for Marine Environmental Sciences (MARUM), University of Bremen, Bremen, Germany, ³GeoZentrum Nordbayern, Universität Erlangen-Nürnberg, Erlangen, Germany, ⁴Faculty of Geosciences, University of Bremen, Bremen, Germany, ⁵Department for Geology and Palaeontology, University of Münster, Münster, Germany

Back-arc spreading centres and related volcanic structures are known for their intense hydrothermal activity. The axial volcanic edifice of Maka at the North Eastern Lau Spreading Centre is such an example, where fluids of distinct composition are emitted at the Maka hydrothermal field (HF) and at Maka South in 1,525–1,543 m water depth. At Maka HF black smoker-type fluids are actively discharged at temperatures of 329°C and are characterized by low pH values (2.79–3.03) and a depletion in Mg (5.5 mmol/kg) and SO₄ (0.5 mmol/L) relative to seawater. High metal (e.g., Fe up to ~6 mmol/kg) and rare Earth element (REE) contents in the fluids, are indicative for a rock-buffered hydrothermal system at low water/rock ratios (2–3). At Maka South, venting of white smoke with temperatures up to 301°C occurs at chimneys and flanges. Measured pH values range from 4.53 to 5.42 and Mg (31.0 mmol/kg), SO₄ (8.2 mmol/L), Cl (309 mmol/kg), Br (0.50 mmol/kg) and Na (230 mmol/kg) are depleted compared to seawater, whereas metals like Li and Mn are typically enriched together with H₂S. We propose a three-component mixing model with respect to the fluid composition at Maka South including seawater, a boiling-induced low-Cl vapour and a black smoker-type fluid similar to that of Maka HF, which is also preserved by the trace element signature of hydrothermal pyrite. At Maka South, high As/Co (>10–100) and Sb/Pb (>0.1) in pyrite are suggested to be related to a boiling-induced element fractionation between vapour (As, Sb) and liquid (Co, Pb). By contrast, lower As/Co (<100) and a tendency to higher Co/Ni values in pyrite from Maka HF likely reflect the black smoker-type fluid. The Se/Ge ratio in pyrite provides evidence for fluid-seawater mixing, where lower values (<10) are the result of a seawater contribution at the seafloor or during fluid upflow. Sulphur and Pb isotopes in hydrothermal sulphides indicate a common metal (loid) source at the two vent sites by host rock leaching in the reaction zone, as also reflected by the REE patterns in the vent fluids.

Keywords: hydrothermal systems in back-arc basins, three-component fluid mixing, vent fluids, hydrothermal sulphides, Northeast Lau basin, trace elements, isotopes

1 INTRODUCTION

Heat loss during the cooling of the oceanic crust is the driver for hydrothermal fluid circulation (e.g., Von Damm, 1995; German and Seyfried, 2013; Humphris and Klein, 2018). Seawater that percolates through the oceanic crust is chemically modified due to water-rock interaction during low temperature alteration (<250°C) in the recharge zone and temperatures up to 400°C in the reaction and upflow zone, where most of the metals are leached (German and Von Damm, 2003; Bach et al., 2013; Humphris and Klein, 2018). In addition to the leaching process, metals may be contributed by magmatic volatiles, as known from island arc and some back-arc hydrothermal systems (de Ronde et al., 2011; Keith et al., 2018; Seewald et al., 2019; Fox et al., 2020; Martin et al., 2020). As the hot (up to 400°C), low pH (2–4) and metal-bearing fluid rises towards the seafloor strong physicochemical gradients (e.g., temperature, pH, redox, ligand availability) lead to the formation of (subsurface) hydrothermal precipitates due to processes like fluid boiling and fluid-seawater mixing (Diehl et al., 2020; Falkenberg et al., 2021; Keith et al., 2021; Schaarschmidt et al., 2021). Previous studies highlighted that fluid boiling is an efficient process for metal fractionation and precipitation in arc and back-arc hydrothermal systems due to temperature-pressure conditions below the critical point of seawater at 408°C and 301.1 bars (i.e., 3,060 m water depth; Stoffers et al., 2006; Monecke et al., 2014). Hence, the complex interplay of temperature-pressure conditions, host rock composition and magmatic volatile influx can produce hydrothermal fluids and related precipitates with a high compositional variability (Von Damm et al., 1985a; Gamo et al., 1997; Koschinsky et al., 2008; Mottl et al., 2011; Reeves et al., 2011; James et al., 2014; Seewald et al., 2015; Wohlgemuth-Ueberwasser et al., 2015; Keith et al., 2016a; Stucker et al., 2017; Kleint et al., 2019; Diehl and Bach, 2020; Martin et al., 2020).

Fluid boiling leads to the physical separation of a fluid into a low-Cl vapour and a high-Cl liquid phase enriched in Cl relative to seawater (539 mmol/kg Cl; Stoffers et al., 2006; Monecke et al., 2014; Schmidt et al., 2017). Depending on their volatility the dissolved elements either partition into the vapour (e.g., As, Sb, Te) or liquid phase (e.g., Fe, Co, Ni) and/or precipitate (e.g., Au) as a consequence of boiling-induced changes in fluid pH, redox, and ligand availability (e.g., Cl, H₂S; Drummond and Ohmoto, 1985; Grundler et al., 2013; Monecke et al., 2014; Pokrovski et al., 2018). Although, liquid-vapour partitioning and precipitation affect fluid chemistry in predictable ways (e.g., Von Damm et al., 1997; Stoffers et al., 2006; Schmidt et al., 2017) it is still unclear how these processes are recorded in the geological archive by sulphide chemistry (Tardani et al., 2017; Román et al., 2019; Keith et al., 2020; Falkenberg et al., 2021; Nestmeyer et al., 2021; Schaarschmidt et al., 2021).

The chemical composition of vent fluids in active systems is highly beneficial for understanding the ongoing hydrothermal processes, but provides only limited information on the temporal evolution of the hydrothermal system (Von Damm et al., 1997; Schmidt et al., 2017; Humphris and Klein, 2018). To date, time-series data from island arcs and adjacent back-arcs are scarce and underrepresented on a global scale, however, recent investigations of hydrothermal fluids and precipitates from the

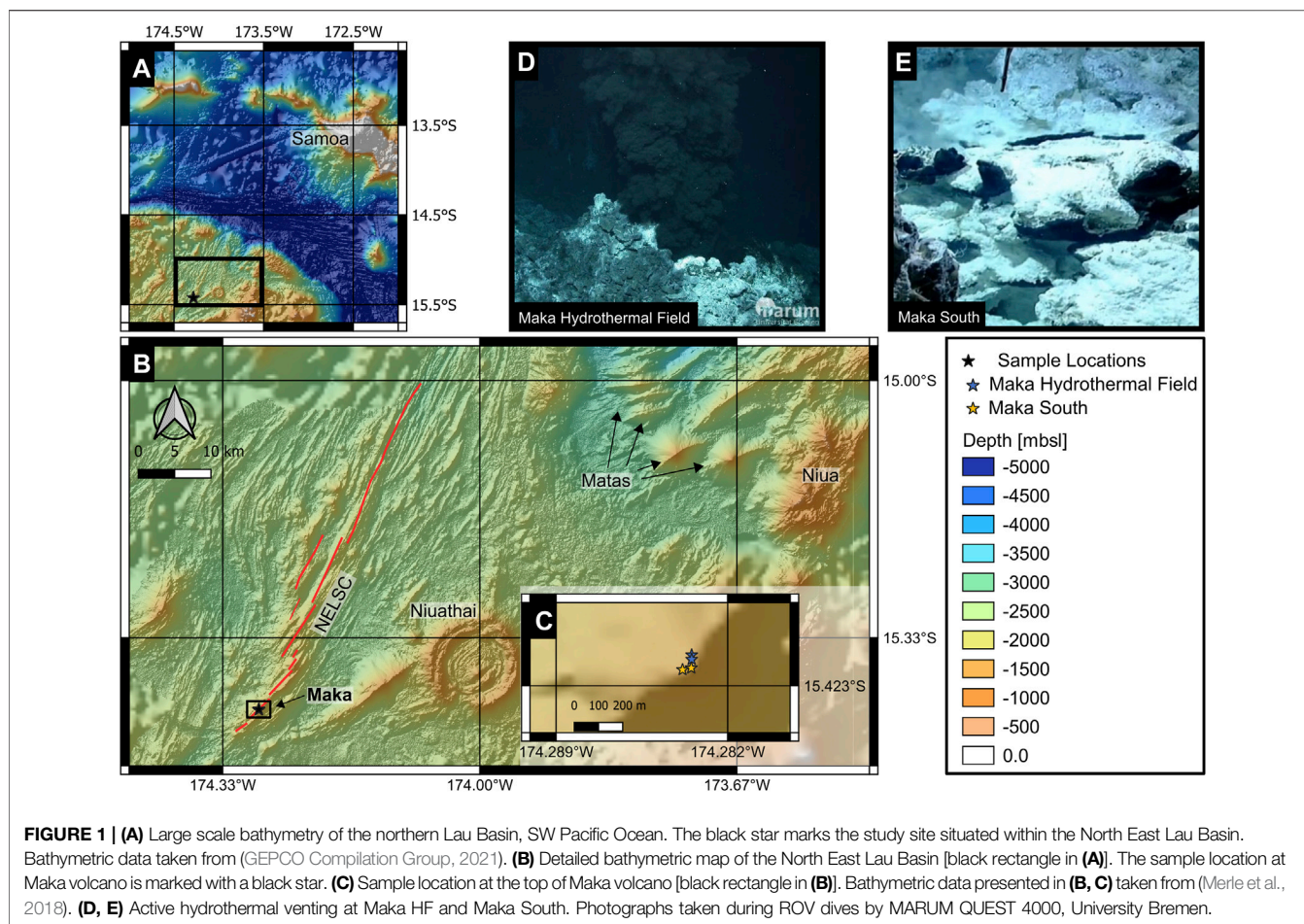
Southwest Pacific, suggest additional short-lived processes (days to months) affecting the geochemical composition of hydrothermal fluids, which is documented by the mineralogy and chemistry of the precipitates from active and inactive vents and chimney talus (Ditchburn et al., 2012; Berkenbosch et al., 2015, 2019; Seewald et al., 2015; Kleint et al., 2019; Diehl et al., 2020; Falkenberg et al., 2021). The complex physical, chemical and temporal aspects that control the chemical composition of hydrothermal fluids also directly influence the associated hydrothermal precipitates (Ditchburn et al., 2012; Keith et al., 2016b; Berkenbosch et al., 2019; Keith et al., 2021). The sampling of submarine hydrothermal vent systems is challenging and in contrast to the fluid compositions that represent a snapshot in time, associated hydrothermal precipitates accumulate and can document changing processes affecting the fluids during the evolution of the hydrothermal system (de Ronde et al., 2011; Fouquet et al., 2018; Berkenbosch et al., 2019; Diehl et al., 2020; Falkenberg et al., 2021).

Here, we report on vent fluid chemistry in combination with *in situ* trace element and isotope data of associated sulphide precipitates from two adjacent vent sites at Maka Volcano, North Eastern Lau Spreading Centre, SW Pacific Ocean. This combined approach provides important new insights into the evolution of submarine hydrothermal systems and the preservation of mixing and boiling in the geological record, as preserved by sulphide chemistry.

2 GEOLOGICAL OVERVIEW AND SAMPLING SITE

The North Eastern Lau Basin in the SW Pacific Ocean (**Figure 1A**) is known for its intense hydrothermal activity and complex tectonic setting (Zellmer and Taylor, 2001; Lupton et al., 2015; Embley and Rubin, 2018; Baker et al., 2019; Baxter et al., 2020; Anderson et al., 2021). The North Eastern Lau Spreading Centre (NELSC, **Figure 1B**) is situated in the western part of the Lau back-arc basin and follows a NE-orientation with an estimated spreading rate of ~42 mm yr⁻¹ (Baxter et al., 2020). It can be subdivided into four segments with the axial Maka volcanic edifice being situated on the southernmost segment (**Figure 1B**, Baker et al., 2011; Anderson et al., 2021). The geochemical composition of the lavas at the NELSC varies from basaltic to dacitic composition, with basaltic compositions dominating at Maka volcano (Haase et al., 2018; Zhang H. et al., 2019).

Maka is the southernmost axial volcanic edifice at the NELSC, where first evidence for hydrothermal activity was indicated by a plume survey in 2004 (German et al., 2006). The first visual confirmation of actively venting high temperature fluids (~315°C) was made by Nautilus Minerals Inc. in 2008 (Baker et al., 2011). Since then, several plume studies focused on southernmost segment of the NELSC, leading to the discovery of eight high-temperature vent sites (German et al., 2006; Kim et al., 2009; Resing et al., 2009; Baker et al., 2011, 2019). At the summit of Maka volcano two active hydrothermal vent sites occur at 1,525–1,543 m water depth (**Figure 1C**), which are characterised



by distinct vent structures and fluid discharge (Figures 1D,E). At the Maka hydrothermal field (Maka HF) vigorously venting black smoker-type fluids with temperatures of up to 329°C (Figure 1D) were observed together with smaller chimneys emitting clear fluids with maximum temperatures of 292°C (Haase et al., 2018). Less than a hundred meters south of Maka HF, a second vent site named Maka South was discovered (Figure 1E), where clear to white fluids are discharged at several sites from flanges and diffuse areas with temperatures between 267 and 301°C (Haase et al., 2018).

3 SAMPLING AND ANALYTICAL METHODS

Sulphide-sulphate samples ($n = 6$) and pillow lavas with fresh glass rims ($n = 4$) were recovered during two dives (Table 1) using the ROV MARUM QUEST 4000 (University of Bremen). Chimney talus (116 ROV-17) and fragments from a 15–20 m high active black smoker (116 ROV-13) emitting high temperature fluids (up to 329°C) were recovered at Maka HF. Samples from flanges discharging white smoke of up to 301°C were sampled at Maka South (122 ROV-17) together with talus material and samples from inactive chimneys (122 ROV-18, 22, 24). Pillow lava samples with glass rims were recovered at Maka HF (116 ROV-09, -07) and

Maka South (122 ROV-09, 10). Hydrothermal fluids were sampled using Isobaric Gas-Tight (IGT) samplers, which were deployed on the ROV. Fluid samples ($n = 6$) were taken after the inlet snorkel was stably positioned and temperature reading on the IGT sampler was constant. After retrieving the sampler, multiple aliquots were sequentially taken from each IGT for on-board analysis of O_2 , H_2S , SO_4 , H_2 and CH_4 concentrations and fluid parameters, such as pH, Eh and salinity (Table 1). Further subsamples were taken for shore-based elemental and isotope analyses of the vent fluids and sulphides (cf. Sections 3.1, 3.2).

3.1 Hydrothermal Sulphide and Volcanic Glass Analysis

3.1.1 Major and Trace Elements

Bulk analyses of sulphide-sulphate samples ($n = 5$) were performed at Activation Labs in Ontario (Canada) using a combination of thermal desorption (TD ICP-MS) and peroxide fusion inductively coupled plasma mass spectrometry (FUS ICP-MS) and instrumental neutron activation analysis (INAA). Detection limits, blanks, analyses of certified reference materials and the analytical results are presented with respect to the different analytical techniques in the supplementary material (Supplementary Table S1).

TABLE 1 | Overview of collected fluid and sulphide samples with maximum fluid temperatures and on-board measured parameters.

Vent field	Sample ID	Water depth (m)	Latitude	Longitude	T _{max} (°C)	T _{mean} (°C)	2 SD (°C)	pH (25°C, 1 atm)	Eh (mV)	Salinity ‰	H ₂ (μmol/l)	CH ₄ (μmol/l)	H ₂ S (μmol/l)
Maka HF	116 ROV-12	1,537	-15.4220	-174.2838	329	322	2.10	3.03	129	35.3	45.6 ±	22.0 ±	11,520
	116 ROV-15	1,528	-15.4222	-174.2838	292	269	24.2	2.79	75.8	32.0	59.6 ± 3.3	45.1 ± 0.1	13,059
	116 ROV-16	1,528	-15.4222	-174.2838				3.33	69.9	33.2	—	—	11,371
Maka South	122 ROV-15	1,525	-15.4225	-174.2838	301	196	67.6	4.53	-47.8	24.8	17.1 ±	25.1 ± 1.2	37,147
	122 ROV-16	1,525	-15.4225	-174.2838	298	258	18.8	5.42	-56.2	31.5	3.31 ± 1.2	5.97 ± 0.2	11,371
	122 ROV-19	1,543	-15.4226	-174.2841	267	183	70.6	4.89	-57.5	29.9	2.5 ± 2.1	40.8 ± 1.1	21,972

Vent Field	Sample ID	Water depth (m)	Latitude	Longitude	Description	—
Maka HF	116 ROV-07	1,649	-15.4199	-174.2819	Vesicular, fresh, glassy crust from pillow/lobate flow	—
	116 ROV-09	1,604	-15.4209	-174.2829	Fresh vesicular pillow fragment with glassy rim	—
	116 ROV-13	1,537	-15.4220	-174.2838	Massive sulphide from active black smoker chimney	—
	116 ROV-17	1,529	-15.4222	-174.2838	Massive sulphide talus	—
Maka South	122 ROV-09	1,579	-15.4233	-174.2853	Porphyritic pillow fragment with glassy rim	—
	122 ROV-10	1,532	-15.4228	-174.2840	Pillow glass rim	—
	122 ROV-17	1,525	-15.4225	-174.2838	Fragment from active chimney	—
	122 ROV-18	1,525	-15.4225	-174.2838	Porous zoned sulphide from inactive chimney	—
	122 ROV-22	1,535	-15.4226	-174.2839	Massive sulphide talus	—
	122 ROV-24	1,523	-15.4226	-174.2837	Massive sulphide talus	—

The trace element composition of volcanic glass samples from Maka ($n = 4$) was determined on hand-picked glass separates by a Thermo Scientific XSERIES 2 Quadrupole ICP-MS at the GeoZentrum Nordbayern (**Supplementary Table S2**). Details about the analytical procedure are presented in Storch et al. (2020).

Major elements in pyrite, chalcopyrite and sphalerite ($n = 113$) were detected by electron probe micro-analysis using a JEOL JXA-8200 Superprobe at the GeoZentrum Nordbayern (**Supplementary Table S3**). For the quantitative analyses, a focused beam with an acceleration voltage of 20 kV and a beam current of 20 nA were used. The following reference materials were used for the standardization: FeS₂ (Fe, S), CuFeS₂ (Cu), ZnS (Zn), InAs (As), Ag₂Te (Ag), CdS (Cd), InSb (Sb), PbTe (Te, Pb) and Au (Au). Data with analytical totals of <98 and >101 wt% were discarded. Each measuring spot was marked on a back-scattered electron image for the subsequent analysis of the same grain by laser ablation inductively coupled plasma mass spectrometry (LA-ICP-MS). Most elements, except Fe, S, Cu and Zn, have concentrations in the trace element range (<0.1 wt%) in pyrite, chalcopyrite and sphalerite, and hence the LA-ICP-MS data were preferentially used for As, Ag, Cd, Sb, Te, Au and Pb.

The trace element analysis of hydrothermal sulphides ($n = 96$) was performed at the GeoZentrum Nordbayern by a Teledyne Analyte Excite 193 nm laser coupled with an Agilent 7500c quadrupole ICP-MS (**Supplementary Table S3**). The mass spectrometer operated with a plasma power

of 1300 W; He (0.9 L/min) and Ar (0.98 L/min) were used as carrier gases. In addition, Ar also acted as plasma (14.9 L/min) and auxiliary gas (0.9 L/min). A single spot ablation pattern with a frequency of 20 Hz and a fluence of 3.5 J/cm² was used. Total analysis time for each spot was set to 45 s including 20 s of gas blank analysis prior to ablation. A beam size of 25 μm and on occasion of 15 μm was used according to the size of the analyzed grain. The following standards were used for the external calibration: Po724 B2 SRM (for Au; Memorial University Newfoundland) and MASS-1 (for V, Mn, Co, Ni, Cu, Zn, Ga, Ge, As, Se, Mo, Ag, Cd, In, Sn, Sb, Te, W, Au, Tl, Pb, Bi). In addition, UQAC-FeS-1 (<https://sulfideslasericpms.wordpress.com>), a homogenous nanopowder of natural sulphides doped with a range of trace elements for matrix-matched analyses of Fe-sulphides, was used as a secondary standard. Analytical precision and accuracy were monitored by repeated analysis of Po724 B2 SRM, MASS-1 and UQAC-FeS1 (**Supplementary Table S4**). The relative standard deviation (RSD) in Po724 B2 SRM and MASS-1 for most elements is <10%, except Au (11.4%), Tl (10.2%) and Pb (10.9%). In the secondary standard (UQAC-FeS1) only Ga (11.9%) and Cd (10.8%) showed RSD values > 10%, which are therefore comparable to the primary standards (**Supplementary Table S4**). Trace element concentrations and detection limits were processed by Glitter (van Achterbergh et al., 2000). Spikes in the time-resolved LA-ICP-MS depth profiles were excluded for the calculation of the trace element concentrations.

3.1.2 Sulphur and Pb Isotopes

Sulphur isotope analysis was conducted at the Westfälische Wilhelms-Universität Münster using Flash EA IsoLink elemental analyzer interfaced to a ThermoScientific Delta V Advantage isotope ratio mass spectrometer (EA-IRMS). The measurements were performed on pyrite ($n = 4$), chalcopyrite ($n = 5$) separates without further chemical treatment (**Supplementary Table S5**). About 100 μg of sulphide powder and 300–500 μg V2O5 were admixed in tin capsules. Measured values are presented in per-mille difference relative to the Vienna-Canyon Diablo Troilite (V-CDT) reference material. Reproducibility, as determined by replicate analyses of the reference material was better than $\pm 0.2\text{‰}$ (1σ).

For the Pb isotope analysis ($n = 4$, **Supplementary Table S5**), 1–5 mg of sulphide powder was dissolved in 0.4 ml aqua regia (50/50 = 6 M HCl/15 M HNO₃) at 80°C in Teflon beakers. After evaporation on a hot plate the material was redissolved in 1 M HCl. Lead was separated from the rock matrix using 100 μL Eichrom Sr-Spec resin. The sample solution was loaded onto the resin and rinsed with 1 M HCl before collecting Pb in 6 M HCl. All reagents were extra distilled and typical procedural blanks for Pb were 50 pg. The chemical sample treatment in advance of the Pb isotope analysis of the volcanic glass fragments was performed according to an established method as described in Haase et al. (2019). Lead isotope measurements were carried out at the GeoZentrum Nordbayern by a Thermo-Fisher Neptune Plus multicollector ICP-MS using a ²⁰⁷Pb/²⁰⁴Pb double spike to correct for instrumental mass fractionation. The double spike, with a ²⁰⁷Pb/²⁰⁴Pb ratio of 0.82, was calibrated against a solution of the NBS981 equal atom Pb standard. Samples were diluted with 2% HNO₃ to a concentration of approximately 20 ppb, and an aliquot of this solution was spiked in order to obtain a ²⁰⁸Pb/²⁰⁴Pb ratio of about 1. Spiked and unspiked sample solutions were introduced into the plasma *via* a Cetac Aridus desolvating nebulizer and measured in static mode. Interference of ²⁰⁴Hg on ²⁰⁴Pb was corrected by monitoring ²⁰²Hg. An exponential fractionation correction was applied offline using the iterative method of Compston and Oversby (1969) with a correction of typically 4.5‰ per amu. The NBS981 Pb isotope standard, measured as an unknown together with the samples yielded ²⁰⁶Pb/²⁰⁴Pb, ²⁰⁷Pb/²⁰⁴Pb, ²⁰⁸Pb/²⁰⁴Pb ratios of 16.9417 ± 0.0001 , 15.4991 ± 0.0001 and 36.7228 ± 0.0002 , respectively. Data are reported relative to our long-term average of the NBS981 Pb standard (16.9410 ± 0.0020 for ²⁰⁶Pb/²⁰⁴Pb, 15.4993 ± 0.0019 for ²⁰⁷Pb/²⁰⁴Pb, 36.7244 ± 0.0046 ²⁰⁸Pb/²⁰⁴Pb).

3.2 Hydrothermal Fluids

3.2.1 On-Board Measurements

The on-board analyses (**Table 1**) for pH, redox potential (Eh), salinity and dissolved oxygen (O₂) were performed using a WTW pH/Cond 340i multimeter. The following sensors were used for the analysis: SenTix ORP platinum electrode with 3M KCl reference electrolyte for Eh, SenTix 41 probe for pH, WTW TetraCon 325 conductivity probe for salinity and optical WTW FDO sensor for O₂. The on-board analysis of dissolved H₂ and

CH₄ was carried out using a headspace extraction method (with gas to liquid volume ratios of >3) and a 7820A Agilent gas chromatograph that operated with N₂ as carrier gas. The gas chromatograph was calibrated with a reference gas containing 253 mol-ppm H₂, 120.1 mol-ppm CH₄, 100.5 mol-ppm CO and 101.1 mol-ppm CO₂. The samples were directly injected after the headspace extraction (including water vapor) and were separated in a Molsieve 60/80 column (Sigma Aldrich, St. Louis, MO) with H₂ and CH₄ being simultaneously detected in a serial set-up of a thermal conductivity detector and a flame-ionization detector, respectively. For each fluid sample with sufficient sample volume the headspace extraction was performed on three individual aliquots to evaluate the precision of the analyses (samples 116 ROV-12 and 122 ROV-15 were exhausted during draw of other aliquots before possible measurement of multiple aliquots). The precision was better than 10% for all samples where multiple aliquots were measured. Concentrations of dissolved H₂S were analysed photometrically following the methylene blue method described by Cline (1969). Dissolved sulphide was initially stabilized in a gelatinous zinc acetate solution, followed by the addition of a colour reagent (N,N'-Dimethyl-1,4-phenylenediamin) and a catalyst (FeCl₃). Photometric measurements were carried out using a ThermoScientific Genesys 10 UV photometer at 660 nm wavelength. The dissolved sulphate (SO₄) concentration was determined gravimetrically by precipitation as insoluble BaSO₄. Volumes of 15–75 ml of the solution were acidified with hydrogen chloride to a pH ≤ 2 , heated to near boiling point temperatures ($\sim 85^\circ\text{C}$) and mixed with BaCl₂ solution (8.5%) to one fifth of the original volume. The BaSO₄ precipitate was subsequently filtered by a pre-weight 0.45 μm cellulose nitrate filter and dried at 40°C.

3.2.2 Major and Trace Elements

The fluid samples were pressure-filtered through 0.2 μm polycarbonate (PC) filters under a laminar flow bench, acidified to pH < 2, using suprapure 30% HCl and stored cool in acid-cleaned PE bottles until further analysis. Concentrations of major and minor elements (B, Br, Cl, Na, Ca, K, Fe, Mn, K, Sr, Li, Mg, Zn, Cu, Si) were determined by inductively coupled plasma – optical emission spectroscopy (ICP-OES, Spectro Ciros), using a matrix-matched calibration at Jacobs University Bremen. Trace and rare Earth elements (REE) were determined by matrix separation following Schmidt et al. (2010) and measured by inductively coupled plasma – mass spectrometry (ICP-MS, Perkin Elmer NexION) at Jacobs University Bremen (**Table 2**, **Supplementary Table S6**). Accuracy for major and minor elements was controlled by repeated measurements of the reference materials IAPSO standard seawater (values from Ocean Scientific International Ltd.) and SLRS-6 (certified values from the National Research Council Canada). As quality control for trace and rare Earth elements, the certified reference materials NASS-7 (National Research Council Canada) and TraceCert (Rare Earth Element Mix for ICP, Sigma Aldrich) were measured alongside the samples. The analytical uncertainty of the measured reference materials was $\pm 5\%$ with respect to the certified value.

TABLE 2 | Major, minor and trace element data together with gas concentrations and stable and radiogenic isotopes in the vent fluids from Maka HF and Maka South. Notation: b.d.: below detection limit.

Vent field	Sample ID	Mg (mmol/kg)	Ba (μmol/kg)	Ca (mmol/kg)	Co (nmol/kg)	Cs (nmol/kg)	Fe (mmol/kg)	K (mmol/kg)	Li (μmol/kg)	Mn (μmol/kg)	Na (mmol/kg)	Pb (nmol/kg)	Rb (μmol/kg)	Si (mmol/kg)	Sr (μmol/kg)	U (nmol/kg)	Zn (μmol/kg)
Maka HF	116 ROV-12	5.52	29.8	47.0	854	1,025	6.05	38.9	282	1,175	382	0.88	97.0	14.8	173	2.84	1.90
	116 ROV-15	6.87	10.6	42.7	90.7	906	5.07	35.2	250	1,050	414	b.d.	84.5	13.3	164	4.02	1.59
	116 ROV-16	13.4	—	38.0	—	—	4.26	31.6	223	920	440	—	—	11.5	150	—	25.8
Maka South	122 ROV-15	31.0	1.90	11.5	21.0	145	b.d.	11.0	54.8	208	230	0.33	12.2	5.99	72.5	5.52	b.d.
	122 ROV-16	46.2	—	11.2	—	—	b.d.	9.85	31.7	47.2	371	—	—	1.50	84.7	—	b.d.
	122 ROV-19	45.4	1.13	8.26	22.5	12.9	b.d.	9.04	22.3	19.5	410	1.00	2.06	2.29	68.8	6.08	b.d.
	SW ^a	52.8	0.13	10.0	0.02	2.14	0.00	9.92	25.8	0.002	464	0.01	1.35	0.125	87.3	13.2	0.054
Vent Field	Sample ID	B (μmol/kg)	Br (mmol/kg)	Cl (mmol/kg)	CO2 (mmol/kg)	SO4 (mmol l-1)	δ11B ± 2SD (‰)	87Sr/86Sr ± 2SD (‰)	δ2HH2O ± 1SD (‰)	δ18OH2O ± 1SD (‰)							
Maka HF	116 ROV-12	705	0.97	529	21.9	0.50	26.0 ± 0.0	0.70440 ± 0.00010	-0.7 ± 1.0	0.88 ± 0.1							
	116 ROV-15	656	0.87	549	29.3	1.60	27.6 ± 0.1	0.70448 ± 0.00001	0.3 ± 1.0	1.05 ± 0.1							
	116 ROV-16	636	0.89	502	—	5.35	—	—	0.2 ± 1.0	0.78 ± 0.1							
Maka South	122 ROV-15	365	0.50	309	23.1	8.20	32.6 ± 0.1	—	-0.9 ± 1.0	0.70 ± 0.1							
	122 ROV-16	435	0.76	463	2.69	16.2	37.4 ± 0.1	—	-0.3 ± 1.0	0.59 ± 0.1							
	122 ROV-19	391	0.73	490	31.0	17.3	—	—	-0.9 ± 1.0	0.20 ± 0.1							
	SW ^a	417	0.827	539	2.26	28.1	39.6	0.70915	-0.1 ± 1.0	-0.17 ± 0.1							

^aDiehl and Bach (2020).

3.2.3 Total Dissolved CO₂

Aliquots for the concentration measurements of CO₂ were transferred in helium-filled and evacuated glass vials for gas chromatographic analyses at the University of Bremen (**Table 2**). The analysis was carried out following a modified procedure after Reeves et al. (2011) with improved headspace-liquid vapour partitioning calculation. Aliquots were acidified with phosphoric acid (25 wt%) to convert dissolved inorganic carbon (DIC) species to CO₂. Subsequently, a Haysep 80/100 column (Sigma-Aldrich, St. Louis, MO) was used with helium as carrier gas in a Thermo Scientific Trace GC Ultra to quantify the CO₂ concentrations. The gas chromatograph was calibrated with pure CO₂ (99.995 vol%) acting as reference gas. A 25 mmol/kg CO₂ standard was measured alongside the samples to verify the measurements. For each sample, two aliquots were measured three times resulting in a precision of better than 5% (on a relative scale). Measurements of the CO₂ standard yielded an average value of 21.8 mmol/kg for the 25 mmol/kg solution suggesting that the accuracy is better than 15%, but also that the sample concentrations may be systematically under-estimated by up to 12%.

3.2.4 Stable and Radiogenic Isotopes

Aliquots of the samples were filtered on-board through 0.2 μm polycarbonate (PC) filters. Afterwards the Sr was separated from the sample matrix using a one-step column with Sr spec as resin. This chemical separation was modified after Pin and Bassin (1992). After separation, the Sr fraction was loaded together with a tantalum emitter onto rhenium filaments and analysed on a ThermoFisher Scientific TRITON Plus thermal ionization mass spectrometer (TIMS) in dynamic mode at MARUM Bremen (**Table 2**). To correct for instrumental mass fractionation, Sr isotope ratios were normalized to 0.1194 ⁸⁶Sr/⁸⁸Sr. The standard reference material NIST SRM 987 was analysed to determine the accuracy of the Sr isotope measurements, yielding 0.71025 ± 0.00002 (2SD_{mean}, n = 3) for ⁸⁷Sr/⁸⁶Sr, which is in agreement with published TIMS values of NIST SRM 987 [0.710250 ± 0.000044 (2SD_{mean}, n = 1,596); <http://georem.mpch-mainz.gwdg.de>].

Boron was separated from the sample matrix using a micro sublimation technique after Wang et al. (2010) and Wilckens et al. (2018). The B isotope analyses were performed by a ThermoFisher Scientific Neptune Plus multicollector-inductively coupled plasma-mass spectrometer (MC-ICP-MS) equipped with a stable introduction system and a high-efficiency x-cone at MARUM Bremen (**Table 2**). The measurements were carried out by the standard-sample-bracketing method using a 100 ng/g B solution and the NIST SRM 951 boric acid reference material as bracketing standard. Boron isotope values are reported in the conventional δ¹¹B (‰) notation relative to NIST SRM 951. The δ¹¹B value of an internal seawater standard (bottom water from SuSu Knolls, +39.6 ± 0.2, 2SD, n = 5) is in agreement with the literature value (+39.6 ± 0.2, 2SD; Foster et al., 2010), validating the sublimation and measurement technique. The

accuracy and precision of the δ¹¹B method was ±0.2‰ (2SD_{mean}, n = 7) for δ¹¹B, obtained by the repeated analysis of NIST SRM 951.

Fluid samples were analyzed for δ¹⁸O and δ²H at the GeoZentrum Nordbayern. The δ¹⁸O analysis was performed by an automated equilibration unit (Gasbench 2; Thermo Fisher Scientific) in continuous flow mode coupled to a Delta plus XP isotope ratio mass spectrometer (Thermo Fisher Scientific). All samples were measured in duplicates and the reported value is the mean value. The δ²H measurements were carried out by liquid injection into a modified high temperature pyrolysis unit (Thermo TC/EA with CTC PAL autosampler) coupled in continuous flow mode to a Delta V plus isotope ratio mass spectrometer (Thermo Fisher Scientific). The TC/EA unit was converted into an online chromium reduction system based on the principle outlined by Morrison et al. (2001). The glassy carbon tube was removed from the TC/EA and the ceramic tube was filled with quartz wool, quartz glass chips and chromium powder (#10147, 99%, -100 mesh, Alfa Aesar, Karlsruhe, Germany). Temperatures were set to 840°C (reactor temperature) and 85°C (GC column). Injection volume was 1.2 μL by using a 10 μL syringe (SGE Analytical Science, Australia). δ¹⁸O and δ²H values are reported in the standard δ-notation in permil (‰) on the VSMOW/SLAP (Standard Light Antarctic Precipitation/Standard Light Antarctic Precipitation) scale by assigning a value of 0 and -55.5‰ (δ¹⁸O) and 0 and -427.5‰ (δ²H) to VSMOW2 and SLAP2, respectively (Brand et al., 2014). For normalization two laboratory standards that were calibrated directly against VSMOW2 and SLAP2, were measured in each run. External reproducibility based on repeated analyses of a control sample was better than 0.1 and 1‰ (±1 sigma) for δ¹⁸O and δ²H, respectively. The data sets were corrected for memory and instrument drift during the run. Sequence setup and post-run correction procedures were adopted from van Geldern and Barth (2012).

3.2.5 Calculation of Hydrothermal End-Members

Compositions of vent fluids may be affected by seawater mixing prior to or during sampling, when the snorkel of the IGT is not fully centred or as a result of complex vent structures, such as the flanges at Maka South (**Figure 1E**). Therefore, fluid end-member compositions (**Supplementary Tables S7, S8**), reflecting the “pure” hydrothermal fluid without a seawater component, were calculated for all fluid samples based on their Mg concentration (**Table 2**) by linear least square regression through seawater values and extrapolation to 0 Mg (**Supplementary Figure S1**; Von Damm et al., 1985b). According to the same method, end-member temperatures were calculated for 0 Mg in the vent fluids. Isenthalpic-isobaric mixing paths were constructed using the temporally averaged fluid temperature during sample intake, the Mg concentration of the hydrothermal fluid, as well as the temperature of seawater and the seawater Mg concentration. The composition- and temperature-dependent isobaric heat capacity was calculated for fluid mixing processes at seafloor pressures using the empirical relationship presented in Driesner (2007) that was applied to the thermodynamic dataset of pure water presented in Haar et al. (1984).

TABLE 3 | Summary of mineral abundances in active and inactive vent samples and in chimney talus from Maka.

Vent field	Sample #	Type	Pyrite			Marcasite		Chalcocopyrite		Sphalerite		Bornite	Covellite	Chalcocite	Barite
			I	II	III	I	II	I	II						
Maka HF	116 ROV-13	Active	A	C	A	M	I	C	I	I	I	I	I	I	I
	116 ROV-17	Chimney talus	A	C	C	C	C	M	I	M	I	I	I	I	I
	116 ROV-17R	Chimney talus	A	C	I	C	I	C	C	I	I	I	I	I	I
Maka South	122 ROV-17	Active	M	I	I	I	I	T	A	I	M	M	M	M	A
	122 ROV-18	Inactive	—	M	I	I	I	D	I	I	M	M	M	M	I
	122 ROV-18R	Inactive	—	C	I	I	I	D	I	M	I	I	I	I	I
	122 ROV-22	Chimney talus	A	C	C	I	I	C	I	I	I	I	I	I	I
	122 ROV-24	Chimney talus	A	C	I	I	I	C	C	I	I	I	I	I	A

T = trace (<1%), M = minor (1–5%), C = common (5–25%), A = abundant (25–50%)

4 RESULTS

4.1 Petrography of Sulphide-Sulphate Samples

Pyrite, chalcocopyrite, sphalerite and marcasite occur throughout the chimney walls in variable proportions (Table 3) and exhibit distinct textures between the outer chimney wall and the central fluid conduit (Figure 2). Colloform pyrite (py I) typically occurs in the outer chimney wall (Figure 2A), where it is associated with sphalerite (sph I) that overgrew barite (Figure 2B). By contrast, chalcocopyrite is only a minor phase in the outer chimney wall and occurs as part of chalcocopyrite-sphalerite (sph I) alternations surrounding pyrite (py I, Figure 2A). Marcasite (mrc I) also occurs in this mineral assemblage typically forming a seam around pyrite (py I, Figures 2C,D). Towards the intermediate chimney wall chalcocopyrite abundances increase, as commonly reflected by chalcocopyrite-sphalerite (sph II) alternations or the occurrence of sub-to euhedral chalcocopyrite that surrounds pyrite (py I, Figures 2E,F). Besides chalcocopyrite, euhedral pyrite (py II) is a common constituent in the intermediate chimney wall (Figure 2G), which is surrounded by pyrite (py III) and marcasite (mrc II). The inner part of the chimney wall near the central fluid conduit is dominated by chalcocopyrite and secondary Cu-sulphides, like bornite, covellite, and chalcocite-digenite that occur in minor amounts particularly in the inactive samples (Figure 2H). Secondary Cu-sulphides were also rarely observed in samples from active chimneys, where they are associated with sphalerite and barite in the outer chimney wall. However, the main mineral assemblage (pyrite, sphalerite, chalcocopyrite) in active and inactive vents and in chimney talus are comparable (Table 3). Similarly, mineral abundances and textures do not vary between Maka HF and South, with the exception of marcasite that only occurs at the former vent site (Table 3).

4.2 Chemistry of Hydrothermal Sulphides and Volcanic Glass

4.2.1 Bulk Sulphide-sulphate Chemistry

The sulphide-sulphate samples from Maka HF and South overlap in their bulk chemical composition. However, differences were observed with respect to the overall compositional range, as reflected by elevated Mn, Co and Bi contents at Maka HF and a tendency towards higher Cu, Zn, Se, Mo, Ag, Cd, Sb and Ba contents (max. values) at Maka South (Figure 3). Compared to other back-arc hydrothermal systems, Maka is enriched in Co and depleted in Ag, Pb and Bi, whereas the contents of most other elements (e.g., Zn, As, Se, Ba, Au) are comparable. In addition, the sulphide-sulphate samples from Maka are enriched in most elements except Mn and Ni compared to pyrite from the same vent site (e.g., Ni, Cu, Zn, Se, Mo and Bi at Maka South) and with respect to the seafloor lavas (except Mn and Ni, Figure 3).

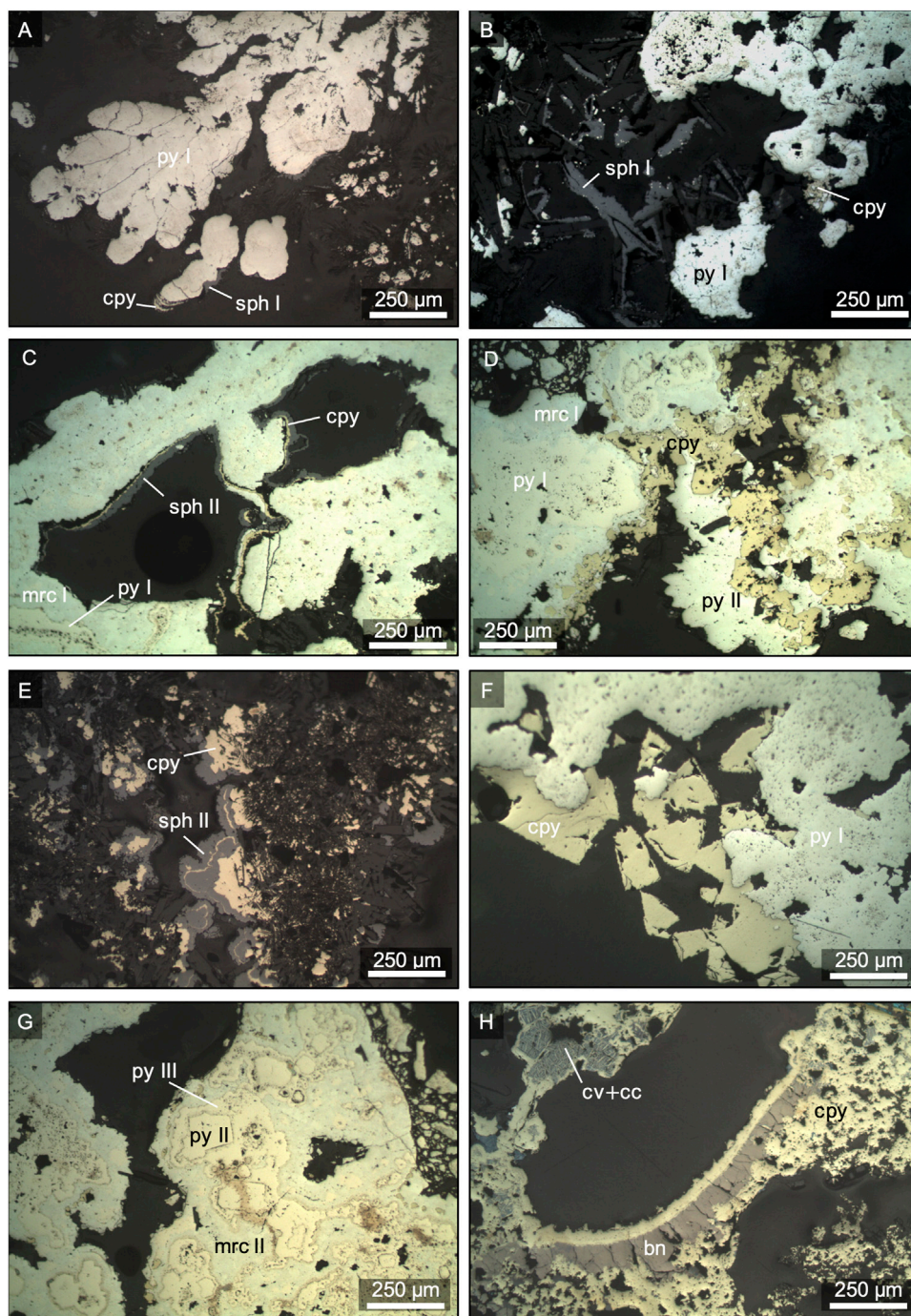


FIGURE 2 | Photomicrographs in reflected light of representative sulphide-sulphate samples from Maka volcano. **(A)** Colloform pyrite I (py I) surrounded by sphalerite I (sph I) and chalcopyrite (cpy, 122 ROV-24, Maka South). **(B)** Sulphide assemblage in the outer chimney wall consisting of pyrite I, sphalerite I and minor chalcopyrite (116 ROV-17R, Maka HF). **(C)** Early pyrite I surrounded by marcasite I (mrc I) and followed by chalcopyrite and late-stage sphalerite II (sph II, 116 ROV-17, Maka HF). **(D)** Pyrite I and marcasite I assemblage surrounded by chalcopyrite and pyrite II of the high temperature stage (116 ROV-17, Maka HF). **(E)** Alternations of chalcopyrite and sphalerite II (122 ROV-24, Maka South). **(F)** Pyrite I surrounded by subhedral chalcopyrite (122 ROV-22, Maka South). **(G)** High temperature euhedral pyrite II associated with late-stage pyrite III (py III) and marcasite II (mrc II, 116 ROV-17, Maka HF). **(H)** Chalcopyrite lining around fluid conduit replaced by supergene bornite (bn), covellite (cv) and chalcocite (cc, 122ROV-18, Maka South). Estimations of mineral abundances in the different samples are presented in **Table 3**.

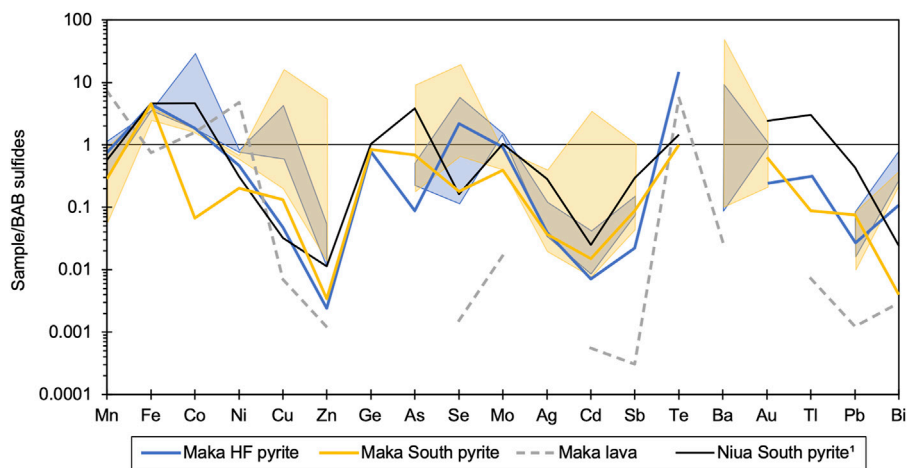


FIGURE 3 | Multi-element diagram comparing the composition of the bulk sulphide-sulphate data from Maka HF and Maka South with the volcanic host rocks, as well as with pyrite from the two vent sites at Maka and from Niua South (Falkenberg et al., 2021). The presented data is normalised to the average bulk composition of back-arc sulphide-sulphate samples (**Supplementary Table S9**).

4.2.2 Major and Trace Elements in Hydrothermal Sulphides

The S and Fe contents of pyrite ($n = 65$) range from 51.1 to 53.8 wt% and 45.3 to 47.3 wt%, respectively. Variations in the major element composition of chalcopyrite ($n = 29$) were observed for S (34.2–35.0 wt%), Fe (29.8–30.4 wt%) and Cu (33.0–34.8 wt%). Differences in the major element composition of pyrite and chalcopyrite between Maka HF and Maka South are insignificant. Sulphur (31.8–33.9 wt%), Fe (0.20–14.1 wt%), Cu (0.01–0.68 wt%) and Zn (50.1–65.4 wt%) in sphalerite are in the major and minor element range. The contents of Fe and Zn in sphalerite show a strong negative correlation ($R^2 = 0.96$, $n = 12$). The sphalerite data can be subdivided into a low-Fe (<2.7 wt%) and a high-Fe (>10.6 wt%) group. Both sphalerite types are present at Maka HF, whereas sphalerite compositions from Maka South are restricted to the low-Fe group (**Supplementary Table S3**).

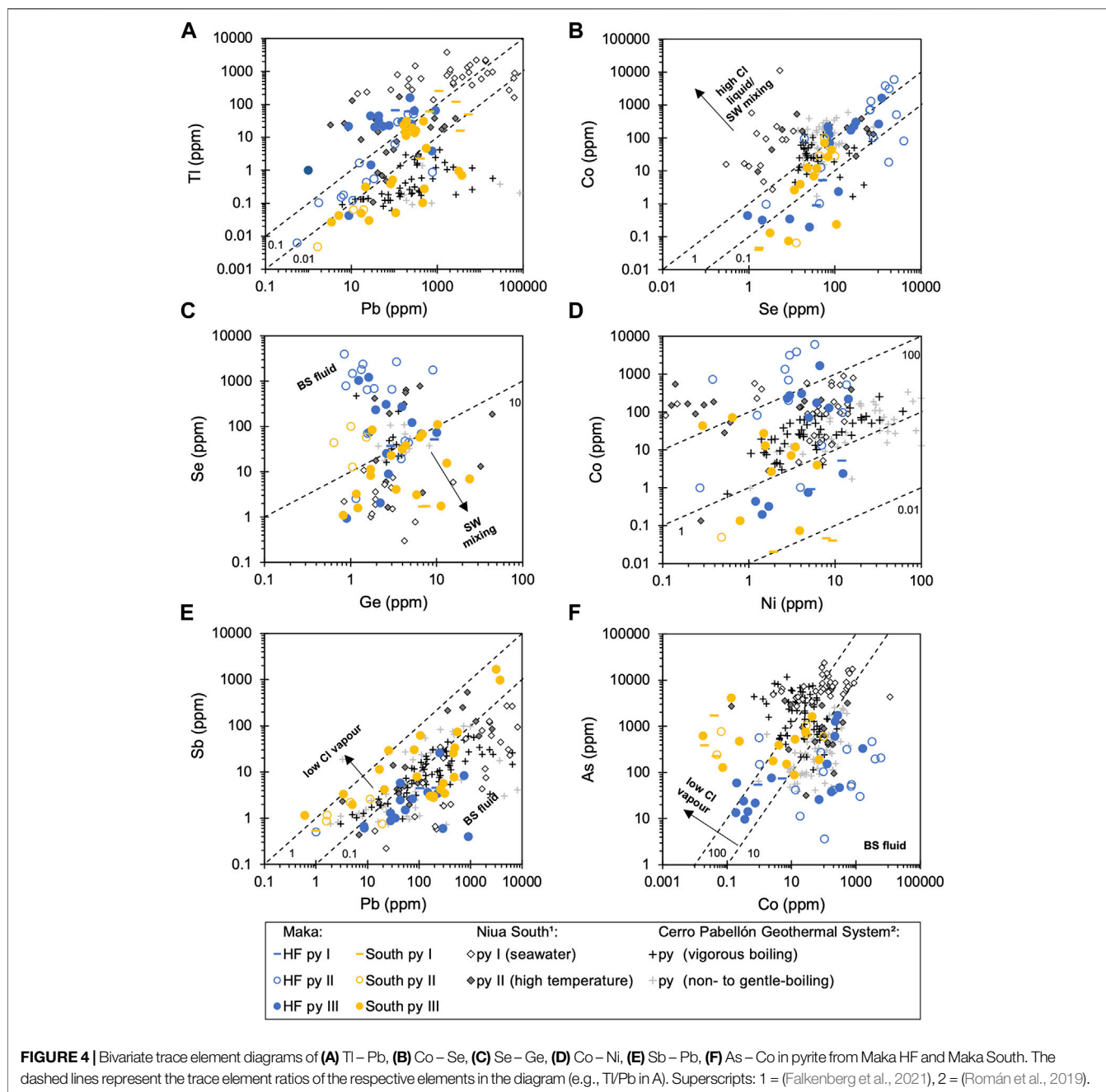
Significant variations were observed in the trace element composition of pyrite between Maka HF and South. On average, pyrite from Maka HF is enriched in Mn, Co, Ni, Se, Mo, Te, Tl and Bi, but depleted in Cu, Zn, As, Cd, Sb, Au and Pb compared to pyrite from Maka South (**Figure 3**). Similar trace element concentrations in pyrite between the two vent sites were observed for Ge and Ag. Compared to pyrite from Niua South (Falkenberg et al., 2021), pyrite from Maka rather exhibits a depleted trace element signature and enrichments compared to the former were only observed for Mn, Ni, Se, Te and Bi at Maka HF and Cu at both vent sites. Hydrothermal pyrite from Maka is enriched in most trace elements, except Mn and Ni, relative to the volcanic glass samples from the seafloor lavas (**Figure 3**).

Trace element variations were also observed between the different pyrite-types (**Figure 4**). Pyrite I tends to show higher Tl and Pb compared to pyrite II (and III) from the same vent site (**Figure 4A**). Pyrite II from Maka HF (and South) is enriched in Co and Se compared to pyrite I and III from

the same vent site (**Figure 4B**). Pyrite III shows a wide compositional range with respect to most trace elements, and therefore overlaps with the data of pyrite I and II (**Figure 4**). Trace element ratios in pyrite between Maka HF and South show systematic variations, such as higher Tl/Pb, Se/Ge (and Co/Ni), as well as lower Sb/Pb and As/Co in pyrite from Maka HF compared to the same pyrite-type from Maka South (**Figure 4**). A negative correlation is described between Co/Ni – As/Co and Se/Ge – As/Co (**Figure 5**), in which respect pyrite from Maka South is characterized by a tendency to higher As/Co (>10), as well as lower Co/Ni (<10) and Se/Ge (<10) ratios (**Figure 5**). Pyrite II from Maka HF generally exhibits the lowest As/Co (<10) and highest Co/Ni (>10) and Se/Ge (>10) ratios. By contrast, pyrite I from Maka South tends to show the highest As/Co (>100) and lowest Co/Ni (<10) and Se/Ge (<10) ratios. Pyrite III from Maka HF and South typically overlap and show intermediate As/Co (10–100), Co/Ni (~10) and Se/Ge (~10) ratios. The observed variations in Co/Ni, As/Co and Se/Ge are most significant between the same pyrite-type from the two vent sites (e.g., Se/Ge – As/Co in pyrite II, **Figure 5B**).

4.2.3 Sulphur and Pb Isotopes in Hydrothermal Sulphides

Sulphur isotope ($n = 9$) values of hydrothermal sulphides from Maka show a narrow range from –0.6 to 1.3‰ compared to other island arc and back-arc vent fields (**Figure 6**, **Supplementary Table S5**). The $\delta^{34}\text{S}$ composition of hydrothermal sulphides from Maka South vary from –0.6 to 1.3‰ and overlap with the compositional range of Maka HF (0.0–0.4‰). With respect to the different hydrothermal sulphides analysed in this study, chalcopyrite (–0.8–1.3‰) tends to show slightly more positive $\delta^{34}\text{S}$ values than the associated pyrite (–0.6–0.0‰, **Supplementary Table S5**). Irrespective of the vent site and the analysed sulphide, the $\delta^{34}\text{S}$ data from Maka shows a compositional range similar to

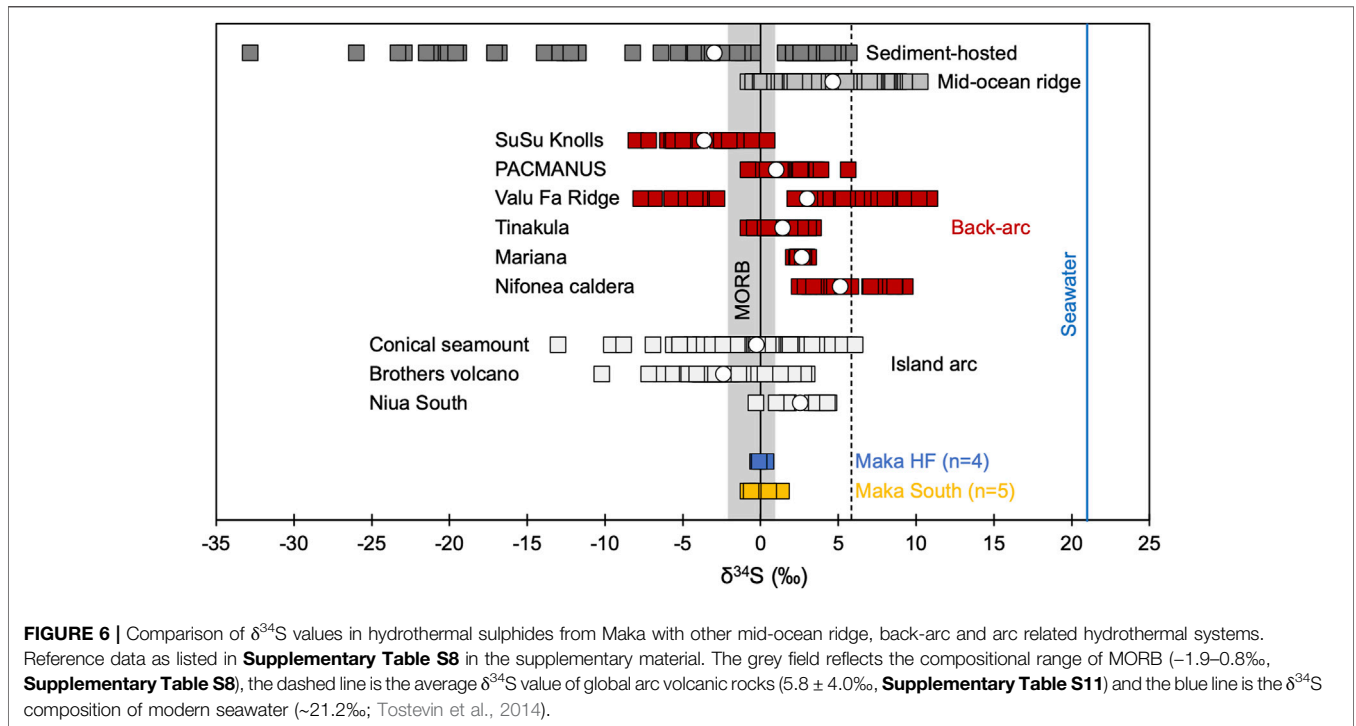
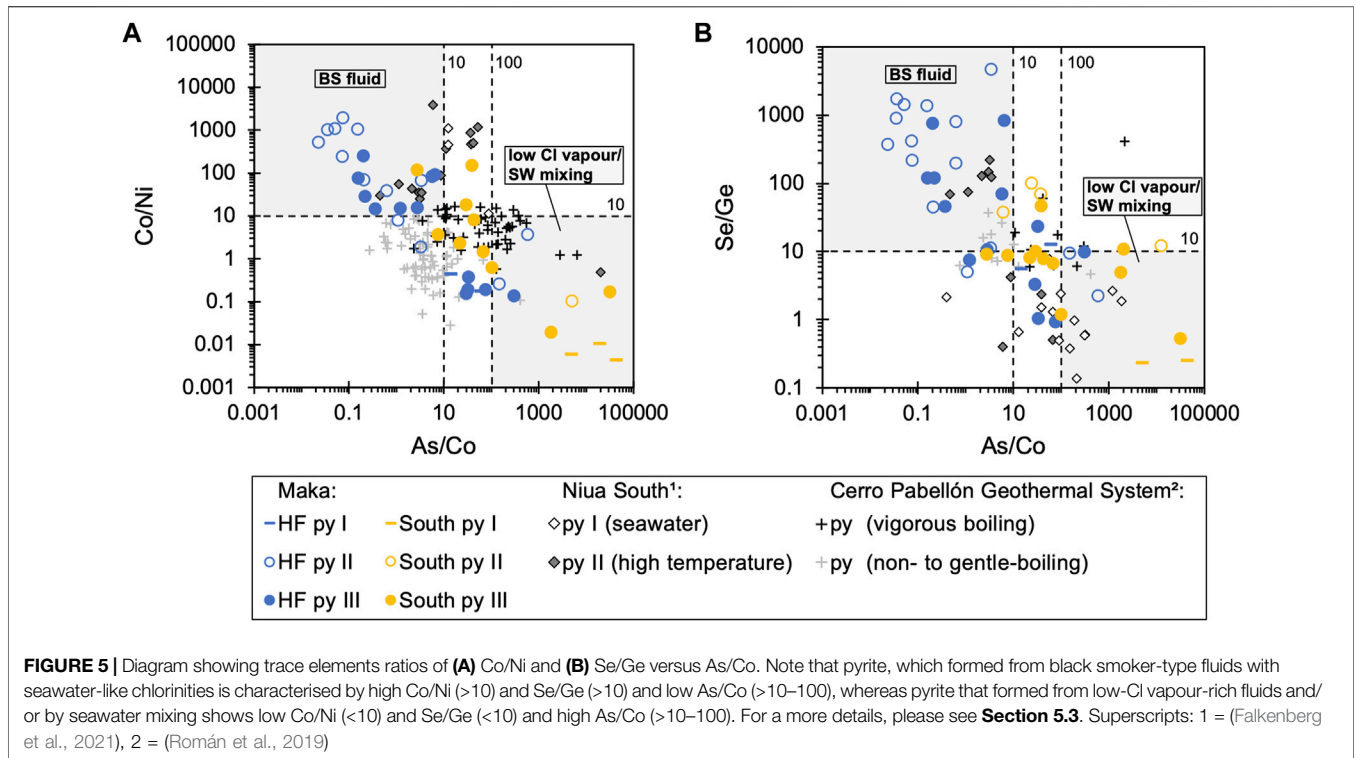


mid-ocean ridge basalt (–1.9–0.8‰; Sakai et al., 1984; Labidi et al., 2012; **Figure 6**).

Variations in the Pb isotope composition of hydrothermal sulphides ($n = 6$) from Maka are minor, as indicated by $^{206}\text{Pb}/^{204}\text{Pb}$, $^{207}\text{Pb}/^{204}\text{Pb}$ and $^{208}\text{Pb}/^{204}\text{Pb}$ values that vary from 18.9474 to 18.9922, 15.6040 to 15.6154 and 38.8399 to 38.8623 (**Supplementary Table S5**). Systematic Pb isotope variations were not observed between the vent sites of Maka HF and South (**Figure 7**), as well as between the analysed pyrite and chalcopyrite separates (**Supplementary Table S5**). The Pb isotope composition of fresh volcanic glass from the seafloor lavas varies from 19.0781 to 19.0849, 15.6169 to 15.6244, 38.9312

to 38.9546 in $^{206}\text{Pb}/^{204}\text{Pb}$, $^{207}\text{Pb}/^{204}\text{Pb}$ and $^{208}\text{Pb}/^{204}\text{Pb}$, respectively (Haase et al., submitted manuscript¹), without showing any systematic variation between the two vent sites. The volcanic glass samples are characterized by more radiogenic Pb isotopes composition than the hydrothermal sulphide separates (**Figure 7**).

¹Haase, K. M., Schoenhofen, M. V., Storch, B., Beier, C., Regelous, M., Rubin, K. H., et al. Effects of the Hydrous Domain in the Mantle Wedge on Magma Formation and Mixing at the Northeast Lau Spreading Centre, SW Pacific. *Geochem. Geophys. Geosys.* submitted manuscript.

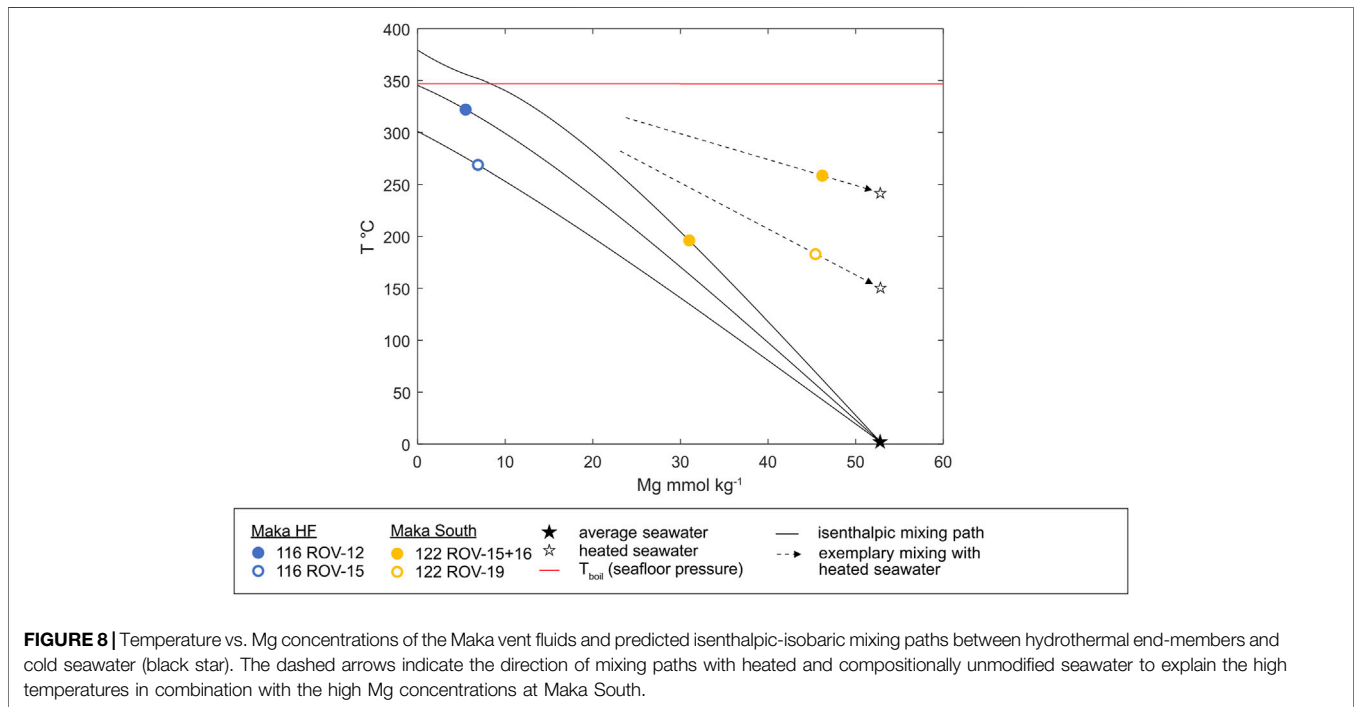
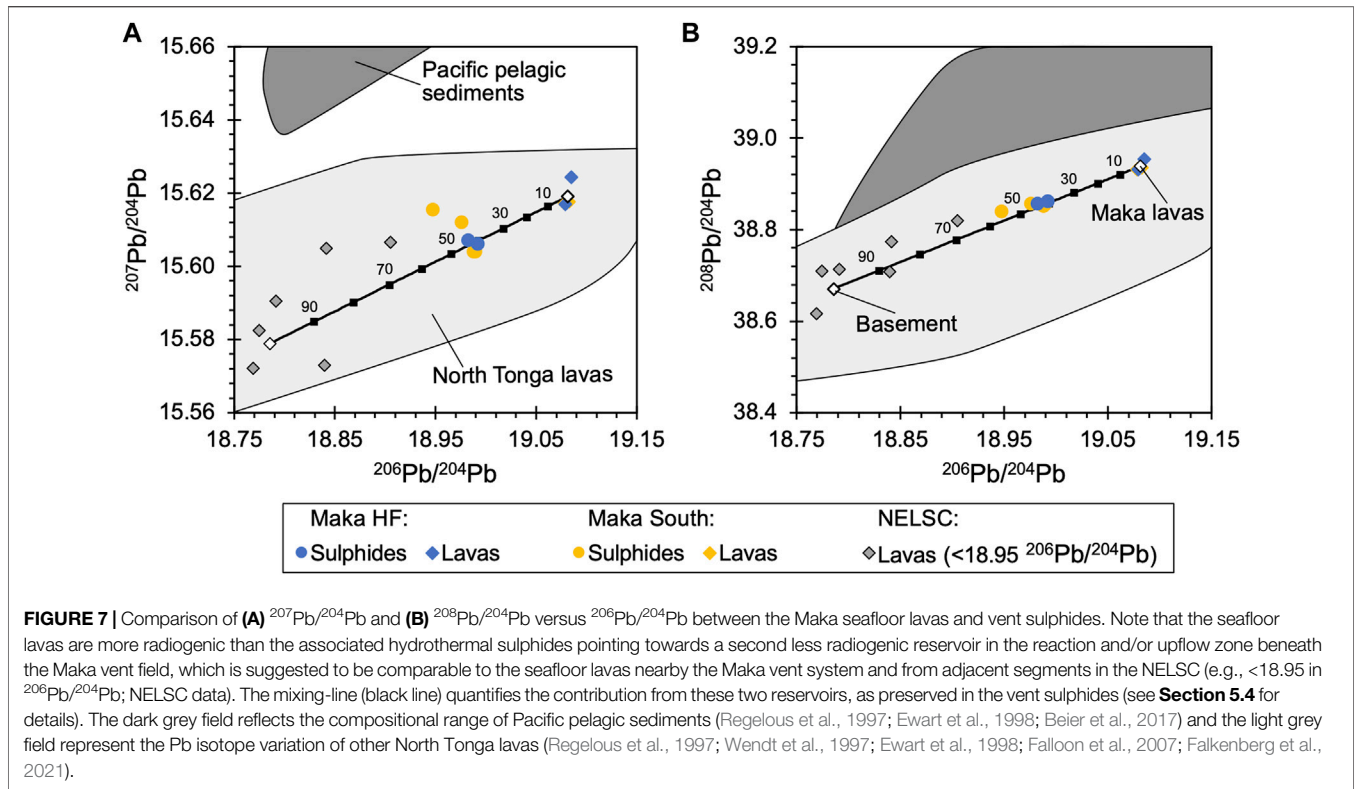


4.3 Chemistry of Vent Fluids

4.3.1 Temperature and pH

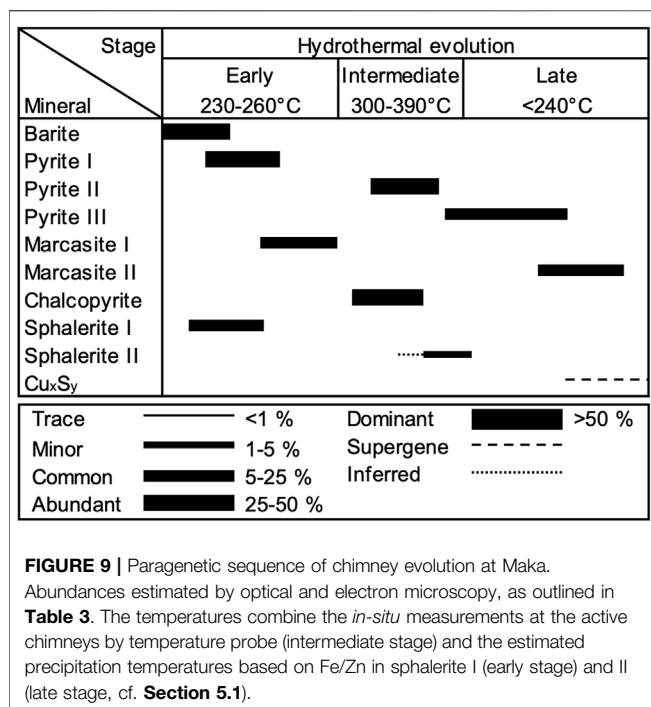
Measured temperatures of black smoker fluids at Maka HF were $322 \pm 2^\circ\text{C}$ (116 ROV-12) and $269 \pm 24^\circ\text{C}$ (116 ROV-15) with peak

temperatures of 329 and 292°C, respectively. At Maka South, measured fluid temperatures from flanges that discharge white and clear fluids were $196 \pm 67.6^\circ\text{C}$ (122 ROV-15), $258 \pm 18.8^\circ\text{C}$ (122 ROV-16) and $183 \pm 70.6^\circ\text{C}$ (122 ROV-19) with peak



temperatures of 301, 298 and 267°C, respectively (Table 1). The calculated temperatures of the end-member fluids are 301–345°C at Maka HF and 379°C at Maka South (Figure 8). End-member

fluid temperatures for Maka South could only be determined for one fluid sample (122 ROV-15), which has the lowest Mg contents (31.0 mmol/kg) at this site (Table 2). The isobaric-



isenthalpic end-member temperature calculations for the other fluid samples from Maka South (122 ROV-16, -19) yielded unreasonably high temperatures (>1,000°C) for a fluid that was affected by mixing with cold ambient seawater (~2°C, **Figure 8**). The measured pH_(25°C, 1 atm) of the Maka South fluids (2.79–3.33) was higher than those from Maka HF (4.53–5.42, **Table 1**).

4.3.2 Major and Trace Elements

At Maka HF, the concentrations of Mg and SO₄ in the hydrothermal fluids vary from 5.52 to 13.4 mmol/kg and 0.50–5.35 mmol/L, respectively (**Table 2**) and are highly depleted compared to seawater (52.8 mmol/kg Mg and 28.1 mmol/L SO₄). The Cl concentrations range from 502 to 549 mmol/kg and are similar to seawater (539 mmol/kg Cl). At Maka South, concentrations of Mg, Cl, Br, Na, Sr, B and U are close to or below seawater concentrations, whereas K, Li, Ca, Mn, Rb, Cs, Ba, Co and Pb are slightly enriched relative to seawater (**Table 2**). The measured H₂S concentrations are highly enriched at Maka South (up to 37,147 μmol L⁻¹) compared to the fluids from Maka HF (up to 13,059 μmol L⁻¹, **Table 1**). By contrast, H₂ concentrations at Maka HF (up to 59.6±3.3 μmol L⁻¹) significantly exceed those from Maka South (up to 17.1 μmol L⁻¹). Measured concentrations of CH₄ and CO₂ in the fluids from both vent sites overlap despite significantly higher Mg concentrations at Maka South (**Tables 1, 2**). The fluids from Maka HF are characterised by higher REE and Y contents compared to those from Maka South (**Supplementary Table S6**). Chondrite-normalized REE patterns of the fluids from both vent sites show an enrichment of light over heavy REEs, as well as a positive Eu anomaly (**Supplementary Figure S2**).

4.3.3 Stable Isotopes

The δ¹¹B values of the vent fluids from Maka HF (26.0–27.6‰) and South (32.6–37.4‰) are distinct and lower than in seawater (39.6‰, **Table 2**). Similarly, the Maka HF fluids are less radiogenic with respect to ⁸⁷Sr/⁸⁶Sr (0.70440–0.70448) compared to seawater (0.70915, **Table 2**). The δ²H_{H₂O} values in the fluids from Maka HF (–0.7–0.2‰) and South (–0.92–0.14) are comparable with respect to the 1 sigma error of the analysis (±1‰, cf. **Section 3.2.4**) and overlap with the seawater composition (–0.14 ± 1.0‰, **Table 2**). By contrast, δ¹⁸O_{H₂O} values are distinct between the two vent sites and compared to seawater (–0.1 ± 0.1‰), as reflected by higher δ¹⁸O_{H₂O} values in the fluids from Maka HF (0.78–1.05‰) compared to those from Maka South (–0.17–0.70‰, **Table 2**).

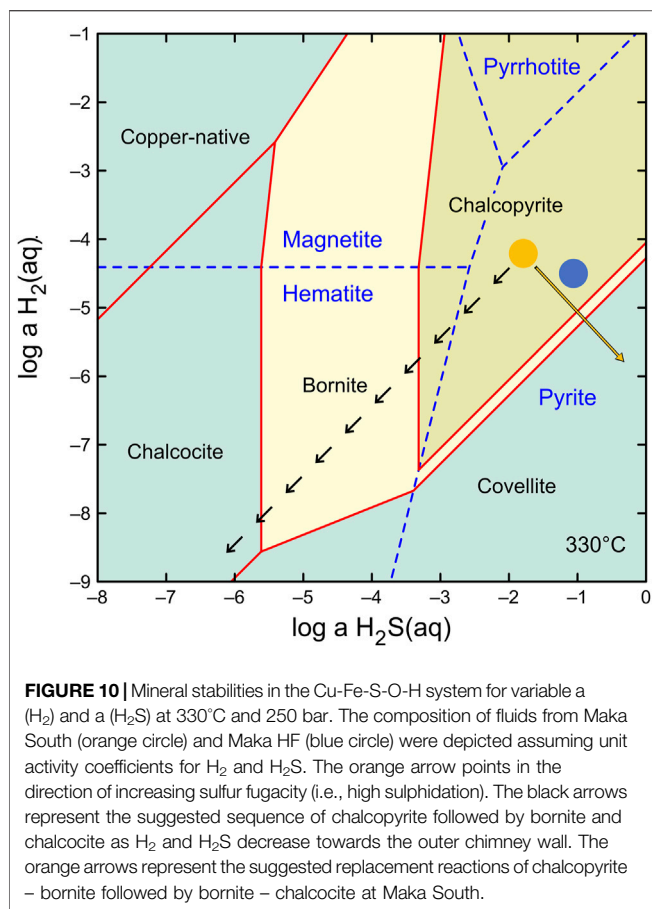
4.3.4 Water/Rock Ratios

In order to estimate the intensity of water-rock (W/R) interaction, the W/R ratios were calculated from end-member fluid compositions (**Supplementary Tables S7, S8**) and metal concentrations measured in fresh volcanic glass from Maka (**Supplementary Table S2**). The W/R ratios were calculated assuming a 100% extraction rate according to the method described by Von Damm et al. (1985b) (for more detail see **Supplementary Table S12**). Fluid-mobile elements, such as Li, Rb, Cs and to a lesser extent K are best suited for determining the W/R ratio, as they are affected only to a small degree by secondary reactions (Mottl and Holland, 1978; Von Damm et al., 1985a). In addition, W/R ratios were also estimated from end-member ⁸⁷Sr/⁸⁶Sr isotopic values following the dissolution first – precipitation second model after Berndt et al. (1988). At Maka HF, the calculated W/R ratios yielded similar results for K, Li, Rb, Cs and ⁸⁷Sr/⁸⁶Sr isotope ratios with values in a narrow range between 2 and 3 (**Supplementary Table S10**).

5 DISCUSSION

5.1 Paragenetic Sequence and Precipitation Conditions

The formation of the vent structures at Maka volcano can be subdivided into an early low temperature (230–260°C), intermediate high temperature (300–390°C) and late low temperature stage (<240°C, **Figure 9**). As a consequence, the mineralogy and precipitation textures vary in the seafloor vents between the different stages reflecting variable fluid conditions (**Figures 2, 9**). The earliest stage of chimney formation is typically related to abundant fluid-seawater mixing leading to the formation of a sulphate-rich (e.g., barite) outer chimney wall with a high permeability for seawater ingress (**Figures 2A,B**; Tivey et al., 1999; Berkenbosch et al., 2012; Webber et al., 2015; Falkenberg et al., 2021; Keith et al., 2021). The formation of early stage colloform and anhedral pyrite I (**Figures 2A,B**), which post-dates the barite deposition is indicative for disequilibrium precipitation conditions due to strong physicochemical



gradients (e.g., temperature) induced by abundant mixing between the hot fluid (290–330°C, **Table 1**) and cold ambient seawater (~2°C; Berkenbosch et al., 2012; Keith et al., 2016a). The precipitation of pyrite I is accompanied by early-stage sphalerite I and marcasite I (**Figures 2B–D**) that likely formed at similar fluid conditions (Murowchick and Barnes, 1986; Metz and Trefry, 2000; Reed and Palandri, 2006). The Fe/Zn ratio of Cu-poor (<2 wt%) sphalerite I can be used to estimate the precipitation temperatures during the early stage (Keith et al., 2014), which are suggested to be in the range of 230–260°C for the Maka hydrothermal system (**Figure 9**). These temperature estimations also agree with the precipitation conditions of marcasite that typically forms at temperatures <240°C (Murowchick and Barnes, 1986; Nestmeyer et al., 2021). This early sulphide precipitation stage insulates the hot ascending fluids in the central conduit from the surrounding seawater leading to higher precipitation temperatures at the onset of the intermediate-stage (**Figure 9**). This is reflected by high temperature phases like chalcopyrite and euhedral pyrite II that form in the intermediate chimney wall (**Figures 2D–G**) and near the central fluid conduit (**Figure 2H**) indicating more stable precipitation conditions with minor seawater mixing (Butler and Nesbitt, 1999; Berkenbosch et al., 2012; Evans et al., 2020; Falkenberg et al., 2021). The onset of sphalerite II formation overlaps with the pyrite II and chalcopyrite

precipitation (**Figures 2E,G, 9**) and temperature estimations based on the Fe/Zn ratio in sphalerite II yielded temperatures between 300 and 390°C (Keith et al., 2014), which are in the range of typical chalcopyrite precipitation temperatures (300–400°C; Butler and Nesbitt, 1999; Metz and Trefry, 2000; Reed and Palandri, 2006). This also agrees with the measured fluid temperatures at Maka HF (up to 329°C), whereas those from Maka South rather tend to be lower (up to 300°C) than the suggested precipitation temperature of sphalerite II (300–390°C). However, minimum concentrations of 31.0 mmol/kg Mg in the Maka South fluids (**Table 2**) are indicative for mixing between fluid and seawater during or prior to fluid sampling, suggesting that the endmember temperatures are >300°C and possibly in the range of the proposed sphalerite II precipitation temperatures (300–390°C), which is confirmed by the suggested endmember fluid temperatures for Maka South that reach 380°C (cf. **Section 4.3.1**). The formation of pyrite III overlaps with sphalerite II (intermediate-stage) and late-stage marcasite II (**Figures 2G, 9**); however, the precipitation of marcasite II continues beyond the pyrite III deposition implying a final decrease in fluid temperature (<240°C, Murowchick and Barnes, 1986; Nestmeyer et al., 2021). This agrees with the late stage occurrence of bornite, covellite and chalcocite-digenite (**Table 3** and **Figure 9**) either indicating a decreasing fluid discharge resulting in seawater ingress caused by a gradient in fluid and seawater pressure in favour of the latter (Tivey, 1995) or a supergene occurrence by chalcopyrite replacement (Berkenbosch et al., 2012; Keith et al., 2016a; 2021). However, marcasite is absent in the bornite, chalcocite-digenite and covellite bearing samples from Maka South (**Table 2**), for which reason we propose that marcasite was not stable under the given fluid conditions probably due to elevated fluid temperatures (>240°C, Murowchick and Barnes, 1986; Nestmeyer et al., 2021). Instead, decreasing a (H_2) and a (H_2S) conditions in high temperature fluids (>300°C) could result in a similar sequence of chalcopyrite followed by bornite and eventually chalcocite/covellite as the activities of H_2 and H_2S decrease towards the outer chimney wall (**Figure 10**), as observed at Maka South. The formation of chalcopyrite and covellite from high temperature fluids can also be related to high-sulphidation conditions (**Figure 10**), where SO_2 is derived from magmatic fluids (Einaudi et al., 2003), for which we do not see evidence at Maka South (cf. **Section 5.4**). However, similar conditions may be achieved by the condensation of boiling-induced vapour into hydrothermal fluids or seawater (Naden et al., 2005; Nestmeyer et al., 2021; Schaarschmidt et al., 2021; Voudouris et al., 2021), as suggested for Maka South (cf. **Sections 5.2, 5.3**). Hence, the paragenetic relations between the different sulphides reflect variations in fluid temperature, a (H_2) and a (H_2S), as well as fluid-seawater mixing in variable proportions and the condensation of boiling induced vapour.

5.2 Fluid Processes and Three-Component Mixing

The Cl concentration of the end-member fluids at Maka HF (524–528 mmol/kg) is comparable to seawater (539 mmol/kg),

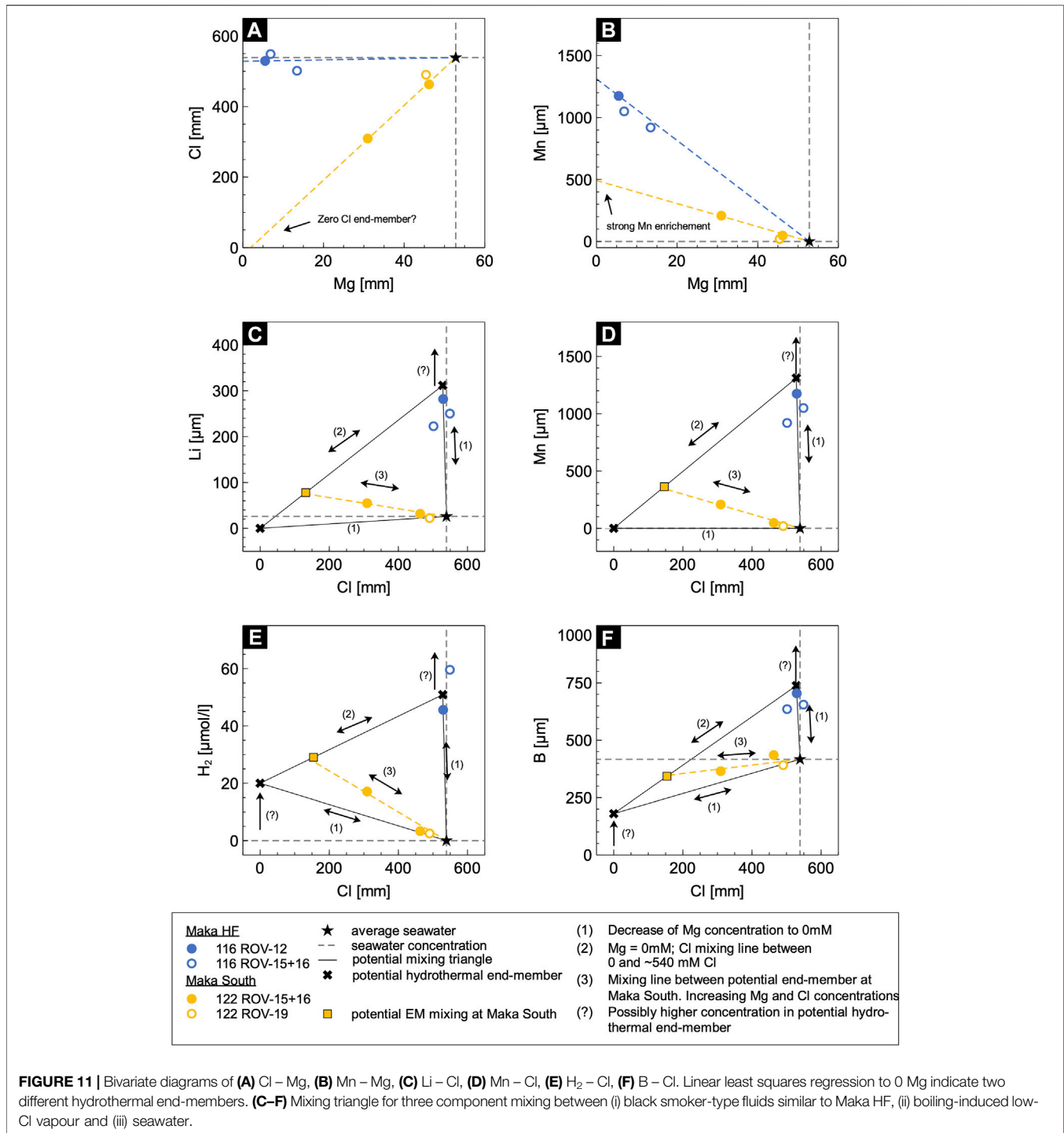
indicating that fluid boiling did not affect the hydrothermal system (**Supplementary Table S7**; Stoffers et al., 2006; Monecke et al., 2014; Schmidt et al., 2017). This interpretation is supported by isenthalpic-isobaric end-member temperature calculations, which yield temperatures between 301°C and 345°C, placing the fluids in the single-phase field below the boiling curve at seafloor pressure (**Supplementary Table S7, Figure 8**). The low Mg and SO₄ concentrations in the sampled fluids from Maka HF indicate that entrainment of seawater prior to or during sampling is minor and that the fluid composition is close to the respective end-member (**Table 2**). The low W/R ratios of 2–3 (cf. **Section 4.3.4**) and overall enrichment of alkali- (e.g. Li, K, Rb), alkali-earth (e.g., Ca, Sr) and rare Earth elements (**Supplementary Tables S7, S8**) relative to seawater suggest a rock-dominated hydrothermal system at Maka HF. Furthermore, lower Na/Cl and higher Ca/Cl ratios in the fluids compared to seawater are indicative for Ca-release from the wall rocks caused by albitization (Berndt et al., 1989; Berndt and Seyfried, 1993). The concentration of dissolved CH₄ (24.6 and 51.8 μmol L⁻¹) is on the lower end of the observed concentration range in hydrothermal fluids from back-arcs (Kawagucci et al., 2011; Reeves et al., 2011, 2014; Seewald et al., 2015) and could either be the result of abiotic sources or microbial activity and thermogenesis of sediments and/or organic matter (Welhan, 1988; Seewald et al., 1994; Cruse and Seewald, 2006; Proskurowski et al., 2008; Fiebig et al., 2019).

The concentrations of dissolved H₂ in the hydrothermal end-member fluids at Maka HF also agree with the low W/R ratios, as H₂ is controlled by fluid-mineral equilibria of Fe-bearing sulphides, oxides and aluminosilicate minerals (Seyfried and Ding, 1995; Seyfried et al., 2003). Stable isotope systematics in the end-member fluids from Maka HF support the interpretation of rock-dominated high-temperature hydrothermal conditions, since δ²H_{H₂O} (up to 0.4‰) and δ¹⁸O_{H₂O} (up to 1.18‰, **Supplementary Table S7** are shifted towards higher values (within analytical uncertainty) compared to seawater (-0.1‰ in δ²H_{H₂O}, -0.2‰ in δ¹⁸O_{H₂O}), which is consistent with seawater-basalt interaction (Shanks et al., 1995; Shanks, 2001). Furthermore, the ⁸⁷Sr/⁸⁶Sr values of the end-member fluids (0.70414) are significantly less radiogenic than seawater (0.70915, **Supplementary Table S7**) and calculated W/R-ratios (2) agree well with those (2–3) based on fluid mobile elements, such as K, Li, Rb and Cs (**Supplementary Table S10**). Likewise, the δ¹¹B values (25.12–26.25) of the end-member fluids are significantly lower than in seawater (39.6, **Supplementary Table S7**), indicating that the boron concentration and δ¹¹B isotope ratios in the vent fluids are controlled by the composition of the host rocks, as suggested for other arc and back-arc hydrothermal systems (Yamaoka et al., 2015; Wilckens et al., 2018). Additionally, fluids venting at Maka HF show chondrite-normalized REE patterns, which overlap with other high-temperature black smoker systems (**Supplementary Figure S2**; e.g., Douville et al., 2002). The observed patterns agree with REE solubilities controlled by chloro-complexation, as is expected for high-temperature systems under rock-dominated redox conditions (e.g.,

Craddock et al., 2010). Hence, the chemistry of the seawater-derived black smoker-type fluids from Maka HF can mainly be attributed to W/R interaction in a rock-dominated non-boiling system with only minor proportions of seawater mixing.

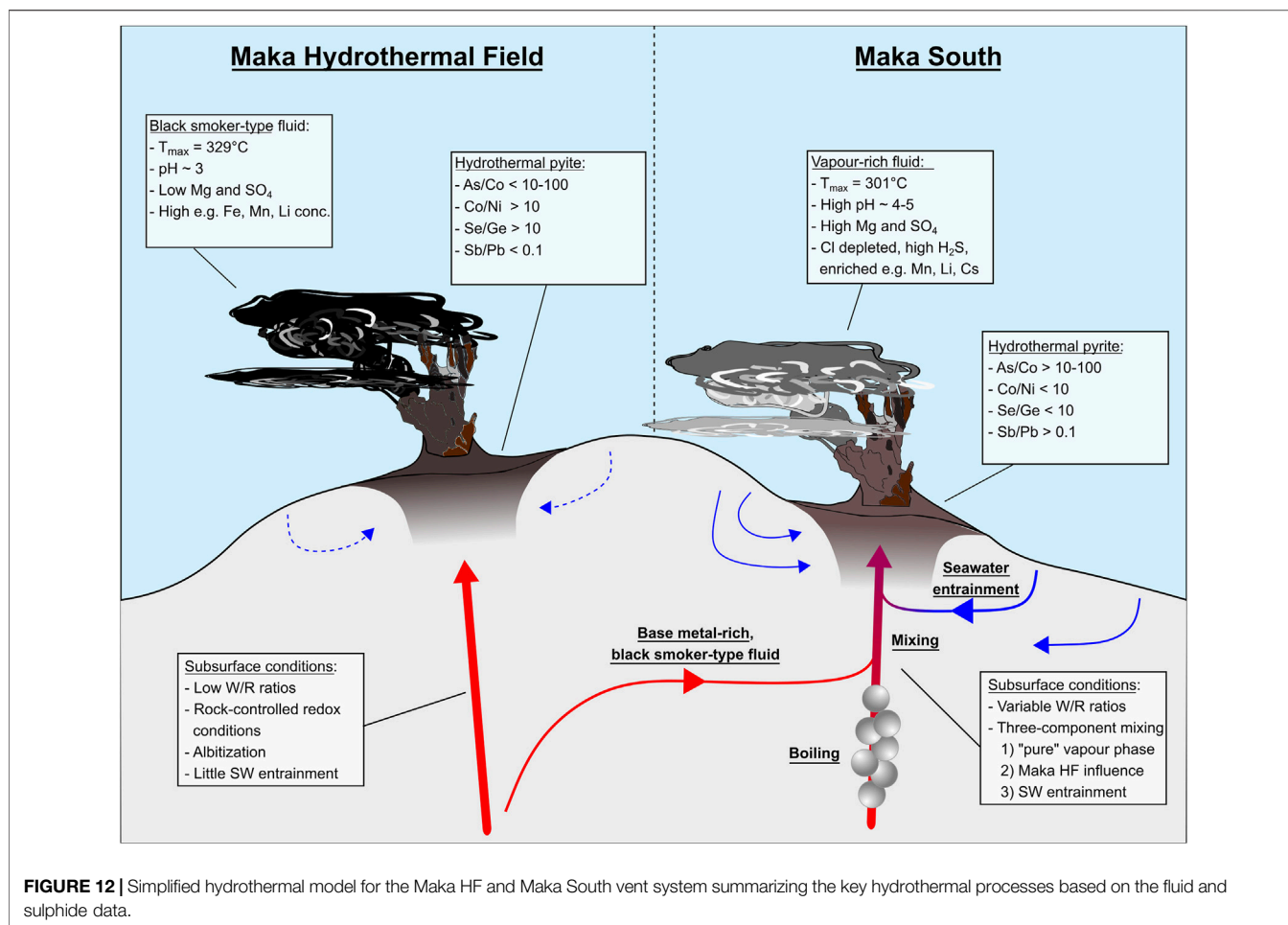
At Maka South, Mg concentrations range from 31.0 to 46.2 mmol/kg (**Table 2**) and together with the elevated pH_(25°C, 1 atm) in the vent fluids (4.53–5.42) seawater mixing prior to or during sampling is suggested. Although the vent fluids from Maka South were sampled at p-T conditions below the boiling curve (**Table 1**), highly variable Cl concentrations (309–490 mmol/kg) that decrease together with the Mg content suggest a low-Cl vapour-rich component in the endmember fluids, which is likely related to subseafloor boiling and subsequent cooling by seawater mixing (Butterfield and Massoth, 1994; Von Damm et al., 1997; James et al., 2014). This is confirmed by isenthalpic-isobaric temperature calculations for end-member fluid compositions that yield temperatures of 379°C (**Supplementary Table S7**), which are above the boiling curve at seafloor pressure, indicating that the fluids intersected the boiling curve in the subseafloor during their ascent (**Figure 8**). Concentrations of Cl, Br, Na and SO₄ versus Mg in the vent fluids show a linear correlation, resulting in negative concentrations of Cl (-20.5 mmol/kg), Na (-117 mmol/kg) and SO₄ (-24.0 mmol/L) in the end-member fluids at 0 Mg (**Supplementary Figure S1, Supplementary Table S7**). These negative concentrations are likely an artefact of the extrapolation to zero-Mg possibly due to the non-conservative behaviour of Mg and other elements during mixing. The low SO₄ concentrations together with the low Ca and Sr contents of the Maka South fluids are indicative for anhydrite precipitation due to subseafloor mixing with entrained seawater. In addition, the negative endmember chloride concentrations also suggest that Mg was probably removed from the mixed fluids, although not as effectively as sulphate. This is consistent with hydrothermal experiments showing that sulphate decreases faster than Mg, when seawater is heated in the presence of basalt to temperatures of 200–300°C (e.g., Seyfried and Mottl, 1982).

It is likely that the Maka South had near 0 mmol/kg Cl prior to mixing and may be interpreted as a “pure” vapour phase that formed by fluid boiling in the subseafloor. Using the SoWat program, the Cl concentration of co-existing vapour and liquid can be calculated in pressure-temperature-composition (p, T, x) space for the NaCl-H₂O system (Driesner, 2007; Driesner and Heinrich, 2007). Assuming a seawater-like chlorinity similar to the black smoker-type fluids from Maka HF (**Supplementary Table S7**), a temperature of 379°C (cf. isenthalpic-isobaric temperature calculations) and variable pressure conditions for subseafloor (~175 bar) boiling yield a vapour phase with ~2 mmol/kg Cl, which agrees with the proposed end-member composition of highly Cl depleted fluids at Maka South (**Supplementary Table S7**) Assuming an equilibrium partitioning of a 1 kg solution with seawater chlorinity, the results also suggest that ~91% low-Cl vapour



(~2 mmol/kg) formed by physical separation from a high-Cl liquid (~9% at ~6,000 mmol/kg Cl). This may also explain the $\delta^2\text{H}_{\text{H}_2\text{O}}$ values of the Maka South fluids (–0.92––0.29), which are more negative than those from Maka HF (–0.67–0.28, **Table 2**). Experimental studies showed that negative $\delta^2\text{H}_{\text{H}_2\text{O}}$ values in vapour-dominated fluids can be the result of open-system boiling, if >90% of a vapour fraction is separated by

boiling during isobaric heating (Shanks et al., 1995; Berndt et al., 1996). Furthermore, boiling leads to the enrichment of dissolved gases (e.g., H₂S, CO₂, CH₄) in the vapour (Drummond and Ohmoto, 1985; Butterfield et al., 1990), which explains the higher gas concentrations in the sampled fluids from Maka South compared to Maka HF (**Table 2** and **Supplementary Table S7**). However, H₂ contents are lower in



the fluids from Maka South than in those from Maka HF, although H_2 is less soluble than H_2S in the aqueous fluid and should hence be even more enriched in the vapor. H_2 may be less controlled by fluid-mineral equilibria of Fe-bearing sulphides, oxides and alumosilicate minerals at the higher W/R ratios at Maka South than at Maka HF. Instead, the compositions are shifted towards higher sulfur fugacities (Kawasumi and Chiba, 2017) (Figure 10), which could point to an influence of the reaction $\text{S}_0 + \text{H}_2 = \text{H}_2\text{S}$. Another possibility is that H_2 partitioned so strongly into the vapour phase that it is already depleted in the boiling fluid, which still release the more soluble gaseous species (e.g., H_2S).

The high Mg contents at Maka South (31.0–46.2 mmol/kg) combined with the low chlorinity and elevated gas contents suggest mixing of a vapour-phase with seawater (Figure 11A). However, this simple mixing scenario cannot explain the enrichment of the Cl-complexed elements Si, Li, K, Ca, Mn, Fe, Co, Rb, Sr, Cs and Pb (Figures 11C,D; Berndt and Seyfried, 1990; Pokrovski et al., 2005) in the Maka South fluids relative to seawater. This observation argues against a simple two-component mixing model between a "pure" vapour phase and seawater, but rather suggests mixing of at least three components; of which one is

enriched in the above mentioned Cl-complexed elements that are leached from the host rocks (Seyfried et al., 1984; Von Damm et al., 1985a; Berger et al., 1988; Berndt and Seyfried Jr, 1990; Seewald and Seyfried Jr, 1990). We propose that this third fluid component is similar in composition to the black smoker-type fluids that are discharged at the nearby vent site (<100 m) of Maka HF. This three-component mixing model is supported by the SO_4 concentrations in the Maka South vent fluids, which significantly depart from a conservative mixing line between seawater and a Mg- and SO_4 -free end-member typically expected for high temperature hydrothermal systems (Supplementary Figure S1E; Mottl and Holland, 1978). Hence, we propose a mixing process between three components for Maka South resulting in a mixing triangle (Figures 11B–E) that includes 1) a black smoker-type fluid that is enriched in alkali-, alkali-earth and trace metals (e.g., Mn, Li, B) 2) a "pure" vapour phase strongly depleted in Cl and enriched in volatile components (e.g., H_2S , CO_2 , CH_4) and 3) a seawater contribution (Figure 12). We suggest that the seawater-derived black smoker-type fluid is derived from the rock-dominated Maka HF system and mixed with the "boiled" vapour-rich fluids in the subseafloor (i.e., vapour sensu stricto or condensed vapour) that were derived from a distinct upflow zone. These fluids then mixed with entrained

and heated seawater in the seafloor or during venting (**Figure 12**) initiating the sulphide precipitation (cf. **Section 5.3**).

5.3 Effects of Fluid Composition on Sulphide Chemistry

Pyrite occurs throughout the paragenetic sequence of chimney formation (**Figure 9**), as indicated by texturally diverse pyrite-types that reflect the different precipitation conditions during the evolution of the Maka hydrothermal system (cf. **Section 5.1**). As a consequence, the trace element composition of the different pyrite-types should report on the fluid composition with respect to the different mineralization stages (**Figure 9**; Wohlgemuth-Ueberwasser et al., 2015; Keith et al., 2016a; Román et al., 2019; Meng et al., 2020; Falkenberg et al., 2021; Nestmeyer et al., 2021). Importantly, trace element concentrations and ratios in pyrite III commonly show a significant variation and overlap with the data of pyrite I and II (**Figure 4**). This is likely related to the precipitation of pyrite III that commences during the intermediate high temperature stage (300–360°C) and which proceeds into the late low temperature stage (<240°C) reflecting conditions similar to the formation of pyrite I and III, respectively (**Figure 9**). The effect of fluid temperature on pyrite precipitation is also preserved by the trace element composition of the different pyrite-types (Huston et al., 1995; Maslennikov et al., 2009; Keith et al., 2016b, 2018; Berkenbosch et al., 2019; Meng et al., 2020; Falkenberg et al., 2021). Pyrite I and III are typically enriched in elements (e.g., Sb, Tl, Pb; **Figures 4A,E**) that are suggested to precipitate at lower fluid temperatures (<250°C; Metz and Trefry, 2000; Reed and Palandri, 2006; Brugger et al., 2016). Similarly, low temperature pyrite I (~240°C) from Niua South that formed due to abundant fluid-seawater mixing during the early stages of chimney growth shows higher Tl and Pb contents than the associated high temperature pyrite II (300–320°C; Falkenberg et al., 2021). By contrast, Se and Co that typically precipitate at elevated temperatures (>300°C Metz and Trefry, 2000; Maslennikov et al., 2009; Berkenbosch et al., 2019; Meng et al., 2020) are enriched in high temperature pyrite II (300–390°C) relative to pyrite I and III from the same vent site at Maka volcano (**Figure 4B**). Other trace elements like Ni, Ge and As in pyrite (**Figures 4C,D,F**) seem to vary irrespective of the precipitation temperature between the different mineralization stages (**Figure 9**). Pyrite-types from the same stage at Maka HF and South probably formed at comparable fluid conditions (e.g., temperature; cf. **section 5.1**), implying that variations in trace element concentrations and ratios are not only related to the seafloor precipitation processes, but are rather also the result of mixing and boiling processes that occur during fluid upflow, which are distinct between the two vent sites, as suggested by the fluid data (cf. **Section 5.2**; Román et al., 2019; Keith et al., 2020; Falkenberg et al., 2021).

Besides temperature, fluid chlorinity also has a significant effect on the solubility of base metals that have an affinity to form Cl-complexes in hydrothermal fluids (e.g., Co, Ni, Zn, Ag, Pb; Metz and Trefry, 2000; Reed and Palandri, 2006; Brugger et al., 2016; Pokrovski et al., 2018). By contrast,

elements with a volatile character (e.g., Sb, Te, As, Tl) may also be soluble at low chlorinities, indicating that their precipitation is not primarily controlled by changes in fluid chlorinity (Grundler et al., 2013; Pokrovski et al., 2018; Román et al., 2019; Keith et al., 2020; Nestmeyer et al., 2021). Metalloids like As and Sb and soft metals (like Au) can be transported by low-Cl fluids with high H₂S, because they tend to form bisulfide complexes (e.g., Akinfiyev and Zotov, 2001). Hence, variations in vent fluid chlorinity and H₂S contents induced by fluid boiling (cf. **Section 5.2**) affect the solubility of metals in the fluids and likely the ratio of volatile to non-volatile elements (e.g., As/Co; Pokrovski et al., 2018). The elevated contents in volatile elements like As, Se, Cd and Sb in some of the bulk sulphide-sulphate samples from Maka South may therefore be related to the low-Cl vapour-rich character of the vent fluids at this site (**Figure 3**). Similarly, previous studies highlighted that boiling signatures and changes in fluid chlorinity may be preserved by the trace element record of pyrite that formed from these fluids (Tardani et al., 2017; Román et al., 2019; Keith et al., 2020; Börner et al., 2021; Falkenberg et al., 2021; Nestmeyer et al., 2021). Nestmeyer et al. (2021) suggested that pyrite from boiling-related low-Cl vapour-rich fluids typically shows higher As/Co ratios (>10–100) due to the preferential partitioning of As into the vapour phase relative to Co that is enriched in the high-Cl liquid. Accordingly, pyrite from Maka South shows higher As/Co ratios (>10–100) than pyrite from Maka HF, which precipitated from black smoker-type fluids with seawater-like chlorinities (524–528 mmol/kg, **Supplementary Table S7**) that are characterized by lower As/Co ratios (<10–100, **Figure 4F**). Importantly, pyrite from Maka HF and those that formed under non-to gentle-boiling conditions from the Cerro Pabellón Geothermal System (CPGS) in Chile show comparable As/Co ratio of <10 to 100 (**Figure 4F**; Román et al., 2019). By contrast, pyrite from the boiling Maka South hydrothermal system overlaps in As/Co with pyrite from the CPGS that formed under vigorous boiling conditions (**Figure 4F**). Similar variations may be observed with respect to Sb/Pb, where pyrite from Maka South tends to show higher Sb/Pb values (>0.1) than pyrite from Maka HF, however, this is not supported by the pyrite data from the CPGS system (**Figure 4E**). Hence, the As/Co (and Sb/Pb) ratio may be a useful tool to distinguish pyrite and related mineralizations that formed from fluids with different chlorinities caused by boiling processes.

The fluid data from Maka South points towards a three-component mixing process involving low-Cl vapours induced by boiling, black smoker-type fluids similar to those from Maka HF and seawater (cf. **Section 5.2** and **Figures 11, 12**). This may also be reflected by the bulk sulphide-sulphate data showing a similar compositional range at both sites, but with a volatile element enrichment (e.g., As, Se, Cd, Sb) in some of the Maka South samples, as described above (**Figure 3**). This is also preserved in the pyrite data from Maka HF and South, as reflected by the compositional overlap in trace element concentrations and ratios between the two vent sites (**Figures 4, 5**). Interestingly, low temperature pyrite I and III (<260°C;

Figure 9) from Maka volcano that are affected by seawater mixing (cf. **Section 5.1**) tend to show the lowest Se/Ge ratios (<10, **Figure 4C**) and those from Maka South overlap with pyrite I from Niua South (Falkenberg et al., 2021), which also precipitated due to intense fluid-seawater mixing as also suggest by the fluid data from Maka South (cf. **Section 5.2**). Hence, the Se/Ge ratio in pyrite may report on mixing processes between hydrothermal fluids and seawater, also indicating that the Se/Ge ratio is not sensitive to boiling-induced fractionation, which is possibly related to the strong tendency of both elements to the vapour phase during fluid boiling likely not affecting their ratio in the fluids and associated pyrite precipitates (Pokrovski et al., 2005, 2018; Brugger et al., 2016).

In addition to the As/Co and Se/Ge in pyrite that are sensitive to fluid boiling and seawater mixing, respectively, the Co/Ni ratio may vary in response to temperature and/or salinity variations in vent fluids (Maslennikov et al., 2009; Brugger et al., 2016; Meng et al., 2020; Falkenberg et al., 2021). Although, there seems to be no clear difference in the Co/Ni value between the different pyrite-types and the two vent sites at Maka (**Figure 4D**), important information may be provided by the combined use of the Co/Ni and As/Co ratio (**Figure 5A**). Here, pyrite II from Maka HF that forms at peak temperatures (300–390°C; **Figure 9**) with only little effect of seawater mixing should best preserve the signature of the black smoker-type fluid, which is characterised by low As/Co (<10) and elevated Co/Ni (>10) possibly reflecting the high temperature and high-Cl (seawater-like) nature of the Maka HF vent fluids (**Figure 5A**). By contrast, the rather low Co/Ni in the Maka South pyrites is therefore more likely related to lower precipitation temperatures due to mixing with seawater (pyrite I and III) or the low-Cl nature of the vapour-dominated fluids at this site, as also suggested by the high As/Co value in the corresponding pyrites (>10–100; **Figure 5A**). This is also supported by the negative Se/Ge - As/Co correlation, where the high temperature black smoker-type fluid related pyrite II from Maka HF shows elevated Se/Ge (>10) compared to pyrite from Maka South, where the combination of the low Se/Ge (<10) and high As/Co (>10–100) are indicative for a mixing process between low-Cl vapours and seawater, as also suggested by the fluid data (cf. **Section 5.2**). Hence, the combined use of trace element ratios in pyrite (e.g., Co/Ni, As/Co, Se/Ge) from seafloor mineralizations (**Figure 5**) may provide important new insights into the complex nature of mixing and boiling processes during fluid upflow; both of which may occur at the same vent site as indicated by the fluid data from Maka South (**Figure 12**).

5.4 Leaching Versus Magmatic Volatile Influx: Evidence by S and Pb Isotopes

The S and Pb isotope composition of the hydrothermal sulphides from Maka HF and South indicate that most of the metals are likely leached from the host rocks in the reaction and upflow zone (**Supplementary Table S5**). Although, the $\delta^{34}\text{S}$ composition of the local host rock at

Maka is unknown the hydrothermal sulphides show $\delta^{34}\text{S}$ values (–0.6–1.3‰) comparable to MORB (–1.9–0.8‰, **Figure 6**; Sakai et al., 1984; Labidi et al., 2012), which is supported by He isotope data ($3\text{He}/^4\text{He} - \text{C}/^3\text{He}$) of volcanic rocks and vent fluids from Maka (and NELSC) also indicating host rock compositions that are comparable to MORB (Lupton et al., 2015; Baker et al., 2019). The lack of more negative $\delta^{34}\text{S}$ values in the hydrothermal sulphides from Maka relative to MORB exclude a contribution of magmatic SO_2 , as known from other subduction zone-related hydrothermal systems (**Figure 6**; Herzig et al., 1998; de Ronde et al., 2011; McDermott et al., 2015; Martin et al., 2020). However, CO_2 concentrations (24.2 and 33.3 mmol/kg) in the end-member fluids are elevated compared to seawater (2.26 mmol/kg, **Supplementary Table S7**) which is commonly related to fluid boiling, W/R interaction, or magmatic volatile influx in sediment-free hydrothermal systems (Reeves et al., 2011; Seewald et al., 2015, 2019) There is no evidence for fluid boiling at Maka HF (cf. **Section 5.2**) and the highest CO_2 concentrations reported for seafloor lavas in the northern Lau Basin (144 ppm or 3.28 mmol/kg; Lupton et al., 2015) can only account for ~3–4 mmol/kg CO_2 in the end-member fluids according to the low W/R ratios of 2–3 at Maka. Therefore, we propose that the Maka hydrothermal system is affected by minor amounts of a CO_2 bearing but almost SO_2 -free magmatic volatile phase. Variable degassing activity is common in volcanically active systems, which are either caused by shallow magma intrusions or permeability changes induced by tectonic movement (Tassi et al., 2013; Acocella et al., 2015). Also, independent and decoupled degassing of magmatically derived CO_2 and SO_2 likely relates to different solubilities at changing p-T and redox conditions in the magma (Gaillard and Scaillet, 2014; de Ronde and Stucker, 2015; Diehl, 2019). As a consequence, most of the reduced S that is incorporated in the seafloor sulphides is either derived from the host rocks due to leaching in the reaction and upflow zone ($\delta^{34}\text{S} = -1.9-0.8\text{‰}$, MORB) or by thermochemical reduction of seawater sulphate ($\delta^{34}\text{S} \sim 21.2\text{‰}$; Tostevin et al., 2014). The S contribution from these reservoirs can be quantified by the two-component mixing equation introduced by Ono et al. (2007). For the calculation only the chalcopyrite data was considered (**Supplementary Table S5**), because only the inner chalcopyrite lining is suggested to be in equilibrium with the vent fluids (McDermott et al., 2015; Evans et al., 2020). We suggest that the contribution of seawater derived S at Maka is <14% and that >86% of the S is leached from the host rocks in the reaction and upflow zone.

Lead in hydrothermal fluids and the associated sulphide precipitates is typically derived by host rock leaching, and thus Pb isotopes of chimney sulphides provide information on the Pb contribution from the surface lavas and different basement rocks in the reaction and upflow zone (Fouquet and Marcoux, 1995; Verati et al., 1999; Zeng et al., 2017; Zhang X. et al., 2019; Falkenberg et al., 2021). Hence, variations in Pb isotope compositions either reflect a contribution from different reservoirs or are the results of radiogenic decay. However, the

very young age of active hydrothermal systems compared to the half-life of the parent isotopes U and Th indicates that effects of radiogenic decay on the Pb isotope composition of hydrothermal sulphides from active seafloor vent systems can be neglected (Zhang X. et al., 2019). Although, the Pb isotope compositions of hydrothermal sulphides from Maka HF and Maka South only vary over a small compositional range, they are distinct with respect to the more radiogenic surface lavas (Figure 7). Hence, a second less radiogenic Pb source in the subsurface, potentially in the reaction zone, is required to explain the Pb isotope variation between the hydrothermal sulphides and the surface lavas (Fouquet and Marcoux, 1995; Falkenberg et al., 2021). Volcanic glass samples from seafloor lavas nearby the Maka vent systems and from adjacent segments along the NELSC revealed Pb isotope compositions that are less radiogenic (e.g., <18.95 in $^{206}\text{Pb}/^{204}\text{Pb}$) than the Maka seafloor sulphides (Figure 7; Haase et al., submitted). Although, the elemental and isotope composition of Pb in crustal rocks beneath the Maka vents is unknown, these samples represent the best possible estimation of this “hidden” Pb reservoir. Thus, a hypothetical two-component mixing-line between the Maka surface lavas and the suggested sub-surface reservoir can be defined (Figure 7). Importantly, the mixing-line intersects the hydrothermal sulphide data indicating that the actual Pb isotope composition of the subsurface rocks that host the hydrothermal system of Maka may be in a comparable range. The combined use of elemental and Pb isotope compositions allows to estimate the Pb contribution from these two reservoirs to the Maka hydrothermal system (Verati et al., 1999). We propose that about 40–50% of the total Pb, as preserved in the seafloor sulphides, was contributed by the “hidden” reservoir in the reaction (or upflow zone). We note that the contribution of Pb derived from seawater mixing can be neglected in this respect due to the highly depleted nature of seawater (0.011 nM Pb; Diehl and Bach, 2020) compared to the volcanic rocks and hydrothermal fluids (Fouquet and Marcoux, 1995; Verati et al., 1999). Hence, the comparison of Pb isotope compositions between fresh seafloor lavas and associated hydrothermal sulphides provides important insights into possible isotope heterogeneities in the oceanic crust (Fouquet and Marcoux, 1995; Verati et al., 1999; Falkenberg et al., 2021). The combined use of S and Pb isotopes indicates that most chalcophile metals at Maka were likely leached from the host rocks and that magmatic volatiles only played a minor role in contributing CO_2 , but without a significant effect on the S budget of the hydrothermal system (Figure 12).

6 SUMMARY AND CONCLUSION

Hydrothermal activity at Maka volcano occurs at two vent sites (Maka HF and Maka South), which are in close proximity to each other. The respective hydrothermal fluids and associated sulphide precipitates show distinct compositions that we attribute to W/R interaction in combination with (subseafloor) boiling and mixing processes. The composition of the vent fluids from Maka HF clearly indicates a W/R-dominated hydrothermal system, where

dissolved metal concentrations are controlled by the chemical exchange between fluid and host rock. This interpretation is supported by S and Pb isotope data of the sulphide precipitates, also indicating that most of the metals are likely leached from the host rocks. The composition of the actively venting fluids at Maka South suggests a complex three-component mixing process during fluid ascent and discharge at the seafloor, which includes 1) a low Cl vapour phase, 2) a base metal-rich black smoker-type fluid similar to those from Maka HF and 3) a contribution by seawater, which we propose is also preserved by the distinct trace element signatures in pyrite from Maka HF and South. Besides the Cl depleted nature of the Maka South vent fluids, evidence for the influence of a vapour-rich phase is given by elevated contents of volatile elements (e.g.; As, Se, Cd, Sb) in bulk sulphide-sulphate samples, as well as higher As/Co ratios (>10 – 100) and Sb/Pb ratios (>0.1) in pyrite from Maka South compared to Maka HF. The influence of a base metal-rich black smoker-type fluid from Maka HF likely leads to the compositional overlap in the trace element data of pyrite from Maka South and Maka HF. Furthermore, a strong seawater entrainment to Maka South is evident by high Mg contents (31.0–46.2 mmol/kg) and high pH values (4.53–5.42) in the measured fluids. Associated pyrite from Maka South shows low Se/Ge ratios (<10) and high As/Co ratios (>10 – 100), which we interpret to be indicative for a mixing processes between low-Cl vapours and seawater. Hence, the combined use of vent fluid and sulphide chemistry allows to define new geochemical tracers in hydrothermal sulphides that can provide important insights into understanding W/R interaction, fluid boiling and seawater mixing during the formation of fossil/extinct seafloor mineralizations that formed under temporally variable fluid conditions.

DATA AVAILABILITY STATEMENT

The original contributions presented in the study are included in the article/Supplementary Material, further inquiries can be directed to the corresponding authors.

AUTHOR CONTRIBUTIONS

LK performed parts of the fluid analyses, interpreted the fluid data, designed parts of the figures and tables, wrote parts of the manuscript; MK supervised the microanalytical study of the sulphide samples, interpreted the sulphide data, designed parts of the figures and tables, wrote parts of the manuscript; DH prepared and investigated the sulphide samples, performed some of the microanalytical analyses; CK, WB, AD, and FW sampled the hydrothermal fluids; WB modelled the mineral stabilities; KH led the research cruise, recovered the sulphide samples; CP, HS performed the S isotope analyses of the sulphides; AD, FW, CP, HS, and RG performed parts of the fluid analyses; RK supervised the LA-ICP-MS laboratory for the sulphide analyses; WB, AK, and KH conceptualized the study; all co-authors reviewed and edited the manuscript.

FUNDING

This work was funded by project 03G0263 of the German Bundesministerium für Bildung und Forschung (BMBF).

ACKNOWLEDGMENTS

We thank Captain O. Meyer and his crew, V. Ratzmeyer and the MARUM ROV team for the excellent support during the scientific

REFERENCES

- Acocella, V., Di Lorenzi, R., Newhall, C., and Scandone, R. (2015). An Overview of Recent (1988 to 2014) Caldera Unrest: Knowledge and Perspectives. *Rev. Geophys.* 53, 849. doi:10.1002/2015rg000492
- Akinfiev, N. N., and Zotov, A. V. (2001). Thermodynamic Description of Chloride, Hydrosulfide, and Hydroxo Complexes of Ag(I), Cu(I), and Au(I) at Temperatures of 25–500°C and Pressures of 1–2000 Bar. *Geochem. Int.* 39, 990–1006.
- Anderson, M. O., Norris-Julseth, C., Rubin, K. H., Haase, K., Hannington, M. D., Baxter, A. T., et al. (2021). Geologic and Structural Evolution of the NE Lau Basin, Tonga: Morphotectonic Analysis and Classification of Structures Using Shallow Seismicity. *Front. Earth Sci.* 9, 1–24. doi:10.3389/feart.2021.665185
- Bach, W., Jöns, N., and Klein, F. (2013). “Metasomatism within the Ocean Crust,” in *Metasomatism and the Chemical Transformation of Rock. Lecture Notes in Earth System Sciences*. Editors D. E. Harlow and H. Austrheim (Berlin/Heidelberg, Germany: Springer), 253–288. doi:10.1007/978-3-642-28394-9_8
- Baker, E. T., Lupton, J. E., Resing, J. A., Baumberger, T., Lilley, M. D., Walker, S. L., et al. (2011). Unique Event Plumes from a 2008 Eruption on the Northeast Lau Spreading Center. *Geochem. Geophys. Geosystems* 12, 1–21. doi:10.1029/2011gc003725
- Baker, E. T., Walker, S. L., Massoth, G. J., and Resing, J. A. (2019). The NE Lau Basin: Widespread and Abundant Hydrothermal Venting in the Back-Arc Region behind a Superfast Subduction Zone. *Front. Mar. Sci.* 6, 1–15. doi:10.3389/fmars.2019.00382
- Baxter, A. T., Hannington, M. D., Stewart, M. S., Emberley, J. M., Breker, K., Krättschell, A., et al. (2020). Shallow Seismicity and the Classification of Structures in the Lau Back-Arc Basin. *Geochem. Geophys. Geosystems* 21, 1–25.
- Beier, C., Turner, S. P., Haase, K. M., Pearce, J. A., Münker, C., and Regelous, M. (2017). Trace Element and Isotope Geochemistry of the Northern and Central Tongan Islands with an Emphasis on the Genesis of High Nb/Ta Signatures at the Northern Volcanoes of Tafahi and Niuaotupapu. *J. Petrol.* 58, 1073–1106. doi:10.1093/ptrology/egx047
- Berger, G., Schott, J., and Guy, C. (1988). Behavior of Li, Rb and Cs during basalt Glass and Olivine Dissolution and Chlorite, Smectite and Zeolite Precipitation from Seawater: Experimental Investigations and Modelization between 50° and 300°C. *Chem. Geology*. 71, 297–312. doi:10.1016/0009-2541(88)90056-3
- Berkenbosch, H. A., De Ronde, C. E. J., Gemmill, J. B., McNeill, A. W., and Goemann, K. (2012). Mineralogy and Formation of Black Smoker Chimneys from brothers Submarine Volcano, Kermadec Arc. *Econ. Geology*. 107, 1613–1633. doi:10.2113/econgeo.107.8.1613
- Berkenbosch, H. A., de Ronde, C. E. J., Paul, B. T., and Gemmill, J. B. (2015). Characteristics of Cu Isotopes from Chalcopyrite-Rich Black Smoker Chimneys at Brothers Volcano, Kermadec Arc, and Niuaotupapu, Lau basin. *Miner. Deposita* 50, 811–824. doi:10.1007/s00126-014-0571-y
- Berkenbosch, H. A., De Ronde, C. E. J., Ryan, C. G., McNeill, A. W., Howard, D. L., Gemmill, J. B., et al. (2019). Trace Element Mapping of Copper- and Zinc-Rich Black Smoker Chimneys from brothers Volcano, Kermadec Arc, Using Synchrotron Radiation XFM and LA-ICP-MS. *Econ. Geol.* 114, 67–92. doi:10.5382/econgeo.2019.4620
- Berndt, M. E., Seal, R. R., Shanks, W. C., and Seyfried, W. E. (1996). Hydrogen Isotope Systematics of Phase Separation in Submarine Hydrothermal Systems:

work onboard RV Sonne. M. Regelous is thanked for help during the Pb-isotope measurements, C. Abe for his assistance during EPMA, and H. Brätz for her support during the LA-ICP-MS study.

SUPPLEMENTARY MATERIAL

The Supplementary Material for this article can be found online at: <https://www.frontiersin.org/articles/10.3389/feart.2021.776925/full#supplementary-material>

- Experimental Calibration and Theoretical Models. *Geochimica et Cosmochimica Acta* 60, 1595–1604. doi:10.1016/0016-7037(96)00033-6
- Berndt, M. E., Seyfried, W. E., and Beck, J. W. (1988). Hydrothermal Alteration Processes at Midocean Ridges: Experimental and Theoretical Constraints from Ca and Sr Exchange Reactions and Sr Isotopic Ratios. *J. Geophys. Res.* 93, 4573–4583. doi:10.1029/jb093ib05p04573
- Berndt, M. E., and Seyfried, W. E., Jr. (1990). Boron, Bromine, and Other Trace Elements as Clues to the Fate of Chlorine in Mid-ocean ridge Vent Fluids. *Geochimica et Cosmochimica Acta* 54, 2235–2245. doi:10.1016/0016-7037(90)90048-p
- Berndt, M. E., and Seyfried, W. E., Jr. (1993). Calcium and Sodium Exchange during Hydrothermal Alteration of Calcic Plagioclase at 400°C and 400 Bars. *Geochimica et Cosmochimica Acta* 57, 4445–4451. doi:10.1016/0016-7037(93)90494-h
- Berndt, M. E., Seyfried, W. E., Jr., and Janecky, D. R. (1989). Plagioclase and Epidote Buffering of Cation Ratios in Mid-ocean ridge Hydrothermal Fluids: Experimental Results in and Near the Supercritical Region. *Geochimica et Cosmochimica Acta* 53, 2283–2300. doi:10.1016/0016-7037(89)90351-7
- Börner, F., Keith, M., Smith, D. J., Barry, T. L., Neumann, T., and Klemm, R. (2021). Fingerprinting Fluid Evolution by Trace Elements in Epithermal Pyrite, Vatukoula Au-Te deposit, Fiji. *Ore Geol. Rev.* 137, 104314. doi:10.1016/j.oregeorev.2021.104314
- Brand, W. A., Coplen, T. B., Vogl, J., Rosner, M., and Prohaska, T. (2014). Assessment of International Reference Materials for Isotope-Ratio Analysis (IUPAC Technical Report). *Pure Appl. Chem.* 86, 425–467. doi:10.1515/pac-2013-1023
- Brugger, J., Liu, W., Etschmann, B., Mei, Y., Sherman, D. M., and Testemale, D. (2016). A Review of the Coordination Chemistry of Hydrothermal Systems, or Do Coordination Changes Make Ore Deposits? *Chem. Geology*. 447, 219–253. doi:10.1016/j.chemgeo.2016.10.021
- Butler, I. B., and Nesbitt, R. W. (1999). Trace Element Distributions in the Chalcopyrite wall of a Black Smoker Chimney: Insights from Laser Ablation Inductively Coupled Plasma Mass Spectrometry (LA-ICP-MS). *Earth Planet. Sci. Lett.* 167, 335–345. doi:10.1016/s0012-821x(99)00038-2
- Butterfield, D. A., and Massoth, G. J. (1994). Geochemistry of north Cleft Segment Vent Fluids: Temporal Changes in Chlorinity and Their Possible Relation to Recent Volcanism. *J. Geophys. Res.* 99, 4951–4968. doi:10.1029/93jb02798
- Butterfield, D. A., Massoth, G. J., McDuff, R. E., Lupton, J. E., and Lilley, M. D. (1990). Geochemistry of Hydrothermal Fluids From Axial Seamount Hydrothermal Emissions Study Vent Field, Juan de Fuca Ridge: Subseafloor Boiling and Subsequent Fluid-Rock Interaction. *J. Geophys. Res.* 95, 921. doi:10.1029/jb095ib08p12895
- Cline, J. D. (1969). Spectrophotometric Determination of Hydrogen Sulfide in Natural Waters I. *Limnol. Oceanogr.* 14, 454–458. doi:10.4319/lo.1969.14.3.0454
- Compston, W., and Oversby, V. M. (1969). Lead Isotopic Analysis Using a Double Spike. *J. Geophys. Res.* 74, 4338–4348. doi:10.1029/jb074i017p04338
- Craddock, P. R., Bach, W., Seewald, J. S., Rouxel, O. J., Reeves, E., and Tivey, M. K. (2010). Rare Earth Element Abundances in Hydrothermal Fluids from the Manus Basin, Papua New Guinea: Indicators of Sub-seafloor Hydrothermal Processes in Back-Arc Basins. *Geochimica et Cosmochimica Acta* 74, 5494–5513. doi:10.1016/j.gca.2010.07.003

- Cruse, A. M., and Seewald, J. S. (2006). Geochemistry of low-molecular weight hydrocarbons in hydrothermal fluids from Middle Valley, northern Juan de Fuca Ridge. *Geochimica et Cosmochimica Acta* 70, 2073–2092. doi:10.1016/j.gca.2006.01.015
- de Ronde, C. E. J., Massoth, G. J., Butterfield, D. A., Christenson, B. W., Ishibashi, J., Ditchburn, R. G., et al. (2011). Submarine Hydrothermal Activity and Gold-Rich Mineralization at Brothers Volcano, Kermadec Arc, New Zealand. *Miner. Deposita* 46, 541–584. doi:10.1007/s00126-011-0345-8
- de Ronde, C. E. J., and Stucker, V. K. (2015). “Seafloor Hydrothermal Venting at Volcanic Arcs and Backarcs,” in *The Encyclopedia of Volcanoes*. Editors H. Sigurdsson, B. Houghton, S. R. McNutt, H. Rymer, and J. Stix (Amsterdam, Netherlands: Elsevier), 823–849. doi:10.1016/b978-0-12-385938-9.00047-x
- Diehl, A. (2019). Causes for Variable Hydrothermal Vent Fluid Compositions in Intraoceanic Arcs: Insights from Fluid Compositions and mineral Precipitates of the South Kermadec Arc. PhD thesis. Bremen, Germany: University of Bremen, 1–170.
- Diehl, A., de Ronde, C. E. J., and Bach, W. (2020). Subcritical Phase Separation and Occurrence of Deep-Seated Brines at the NW Caldera Vent Field, Brothers Volcano: Evidence from Fluid Inclusions in Hydrothermal Precipitates. *Geofluids* 2020, 1–22. doi:10.1155/2020/8868259
- Ditchburn, R. G., De Ronde, C. E. J., and Barry, B. J. (2012). Radiometric Dating of Volcanogenic Massive Sulfides and Associated Iron Oxide Crusts with an Emphasis on ²²⁶Ra/Ba and ²²⁸Ra/²²⁶Ra in Volcanic and Hydrothermal Processes at Intraoceanic Arcs. *Econ. Geology* 107, 1635–1648. doi:10.2113/econgeo.107.8.1635
- Douville, E., Charlou, J. L., Oelkers, E. H., Bienvenu, P., Jove Colon, C. F., Donval, J. P., et al. (2002). The Rainbow Vent Fluids (36°14'N, MAR): the Influence of Ultramafic Rocks and Phase Separation on Trace Metal Content in Mid-Atlantic Ridge Hydrothermal Fluids. *Chem. Geology* 184, 37–48. doi:10.1016/s0009-2541(01)00351-5
- Driesner, T., and Heinrich, C. A. (2007). The System H₂O–NaCl. Part I: Correlation Formulae for Phase Relations in Temperature–Pressure–Composition Space from 0 to 1000°C, 0 to 5000bar, and 0 to 1 XNaCl. *Geochimica et Cosmochimica Acta* 71, 4880–4901. doi:10.1016/j.gca.2006.01.033
- Driesner, T. (2007). The System H₂O–NaCl. Part II: Correlations for Molar Volume, Enthalpy, and Isobaric Heat Capacity from 0 to 1000°C, 1 to 5000bar, and 0 to 1 XNaCl. *Geochimica et Cosmochimica Acta* 71, 4902–4919. doi:10.1016/j.gca.2007.05.026
- Drummond, S. E., and Ohmoto, H. (1985). Chemical Evolution and mineral Deposition in Boiling Hydrothermal Systems. *Econ. Geol.* 80, 126–147. doi:10.2113/gsecongeo.80.1.126
- Einaudi, M. T., Hedenquist, J. W., and Inan, E. E. (2003). Sulfidation State of Fluids in Active and Extinct Hydrothermal Systems: Transitions from Porphyry to Epithermal Environments. *Econ. Geol.* 10, 285–314.
- Embley, R. W., and Rubin, K. H. (2018). Extensive Young Silicic Volcanism Produces Large Deep Submarine Lava Flows in the NE Lau Basin. *Bull. Volcanol.* 80, 1–23. doi:10.1007/s00445-018-1211-7
- Evans, G. N., Tivey, M. K., Montealeone, B., Shimizu, N., Seewald, J. S., and Rouxel, O. J. (2020). Trace Element Proxies of Seafloor Hydrothermal Fluids Based on Secondary Ion Mass Spectrometry (SIMS) of Black Smoker Chimney Linings. *Geochimica et Cosmochimica Acta* 269, 346–375. doi:10.1016/j.gca.2019.09.038
- Ewart, A., Collerson, K. D., Regelous, M., Wendt, J. I., and Niu, Y. (1998). Geochemical Evolution within the Tonga-Kermadec-Lau Arc-Back-Arc Systems: The Role of Varying Mantle Wedge Composition in Space and Time. *J. Petrology* 39, 331–368. doi:10.1093/ptro/39.3.331
- Falkenberg, J. J., Keith, M., Haase, K. M., Bach, W., Klemd, R., Strauss, H., et al. (2021). Effects of Fluid Boiling on Au and Volatile Element Enrichment in Submarine Arc-Related Hydrothermal Systems. *Geochimica et Cosmochimica Acta* 307, 105–132. doi:10.1016/j.gca.2021.05.047
- Falloon, T. J., Danyushevsky, L. V., Crawford, T. J., Maas, R., Woodhead, J. D., Eggins, S. M., et al. (2007). Multiple Mantle Plume Components Involved in the Petrogenesis of Subduction-Related Lavas from the Northern Termination of the Tonga Arc and Northern Lau Basin: Evidence from the Geochemistry of Arc and Backarc Submarine Volcanics. *Geochem. Geophys. Geosystems* 8, 1–45. doi:10.1029/2007gc001619
- Fiebig, J., Stefánsson, A., Ricci, A., Tassi, F., Viveiros, F., Silva, S., et al. (2019). Abiogenesis Not Required to Explain the Origin of Volcanic-Hydrothermal Hydrocarbons. *Geochem. Persp. Lett.* 11, 23–27. doi:10.7185/geochemlet.1920
- Foster, G. L., Pogge Von Strandmann, P. A. E., and Rae, J. W. B. (2010). Boron and Magnesium Isotopic Composition of Seawater. *Geochem. Geophys. Geosystems* 11, 1–10. doi:10.1029/2010gc003201
- Fouquet, Y., and Marcoux, E. (1995). Lead Isotope Systematics in Pacific Hydrothermal Sulfide Deposits. *J. Geophys. Res.* 100, 6025–6040. doi:10.1029/94jb02646
- Fouquet, Y., Pelleter, E., Konn, C., Chazot, G., Dupré, S., Alix, A. S., et al. (2018). Volcanic and Hydrothermal Processes in Submarine Calderas: The Kulo Lasi Example (SW Pacific). *Ore Geology. Rev.* 99, 314–343. doi:10.1016/j.oregeorev.2018.06.006
- Fox, S., Katzir, Y., Bach, W., Schlicht, L., and Glessner, J. (2020). Magmatic Volatiles Episodically Flush Oceanic Hydrothermal Systems as Recorded by Zoned Epidote. *Commun. Earth Environ.* 1, 1–9. doi:10.1038/s43247-020-00051-0
- Gaillard, F., and Scaillet, B. (2014). A Theoretical Framework for Volcanic Degassing Chemistry in a Comparative Planetology Perspective and Implications for Planetary Atmospheres. *Earth Planet. Sci. Lett.* 403, 307–316. doi:10.1016/j.epsl.2014.07.009
- Gamo, T., Galtier, N., Gouy, M., and Gautier, C. (1997). Acidic and Sulfate-Rich Hydrothermal Fluids from the Manus Back-Arc basin, Papua New Guinea. *Geology* 25, 543–548. doi:10.1130/0091-7613(1997)025<0543:aaahrf>2.3.co;2
- GEPCO Compilation Group (2021). GEBCO 2021 Grid. doi:10.5285/c6612cbe-50b3-0c9f-e053-6c86abc09f8f
- German, C. R., Baker, E. T., Connelly, D. P., Lupton, J. E., Resing, J., Prien, R. D., et al. (2006). Hydrothermal Exploration of the Fonualei Rift and Spreading Center and the Northeast Lau Spreading Center. *Geochem. Geophys. Geosystems* 7, 1–15. doi:10.1029/2006gc001324
- German, C. R., and Seyfried, W. E. (2013). “Hydrothermal Processes,” in *Treatise on Geochemistry*. Editors H. D. Holland and K. K. Turekian (Amsterdam, Netherlands: Elsevier), 8, 191–233.
- German, C. R., and Von Damm, K. L. (2003). “Hydrothermal Processes,” in *Treatise on Geochemistry*. Editors H. D. Holland and K. K. Turekian (Amsterdam, Netherlands: Elsevier), 6, 181–222. doi:10.1016/b0-08-043751-6/06109-0
- Grundler, P. V., Brugger, J., Etschmann, B. E., Helm, L., Liu, W., Spry, P. G., et al. (2013). Speciation of Aqueous Tellurium(IV) in Hydrothermal Solutions and Vapors, and the Role of Oxidized Tellurium Species in Te Transport and Gold Deposition. *Geochimica et Cosmochimica Acta* 120, 298–325. doi:10.1016/j.gca.2013.06.009
- Haar, L., Gallagher, J. S., and Kell, G. S. (1984). *NBS/NRC Steam Tables: Thermodynamic and Transport Properties and Computer Programs for Vapour and Liquid States of Water in SI Units*. London, England: Hemisphere Publishing Corporation.
- Haase, K. M., Beier, C., Bach, W., Kleint, C., Anderson, M., Büttner, H., et al. (2018). *RV Sonne Cruise Report (SO263) Tonga Rift*, 1–194. doi:10.13140/RG.2.2.23035.16169
- Haase, K. M., Regelous, M., Schöbel, S., Günther, T., and de Wall, H. (2019). Variation of Melting Processes and Magma Sources of the Early Deccan Flood Basalts, Malwa Plateau, India. *Earth Planet. Sci. Lett.* 524, 115711. doi:10.1016/j.epsl.2019.115711
- Herzig, P. M., Hannington, M. D., and Arribas Jr., A. (1998). Sulfur Isotopic Composition of Hydrothermal Precipitates from the Lau Back-Arc: Implications for Magmatic Contributions to Seafloor Hydrothermal Systems. *Mineralium Deposita* 33, 226–237. doi:10.1007/s001260050143
- Humphris, S. E., and Klein, F. (2018). Progress in Deciphering the Controls on the Geochemistry of Fluids in Seafloor Hydrothermal Systems. *Annu. Rev. Mar. Sci.* 10, 315–343. doi:10.1146/annurev-marine-121916-063233
- Huston, D. L., Sie, S. H., Suter, G. F., Cooke, D. R., and Both, R. A. (1995). Trace Elements in Sulfide Minerals from Eastern Australasian Volcanic-Hosted Massive Sulfide Deposits; Part I, Proton Microprobe Analyses of Pyrite, Chalcopyrite, and Sphalerite, and Part II, Selenium Levels in Pyrite; Comparison with delta ³⁴S Values and Implications for the Source of Sulfur in Volcanogenic Hydrothermal Systems. *Econ. Geol.* 90, 1167–1196. doi:10.2113/gsecongeo.90.5.1167
- James, R. H., Green, D. R. H., Stock, M. J., Alker, B. J., Banerjee, R., Cole, C., et al. (2014). Composition of Hydrothermal Fluids and Mineralogy of Associated

- Chimney Material on the East Scotia Ridge Back-Arc Spreading centre. *Geochim. Cosmochim. Acta* 139, 7–71. doi:10.1016/j.gca.2014.04.024
- Kawagucci, S., Chiba, H., Ishibashi, J.-I., Yamanaka, T., Toki, T., Muramatsu, Y., et al. (2011). Hydrothermal Fluid Geochemistry at the Iheya North Field in the Mid-okinawa Trough: Implication for Origin of Methane in Subseafloor Fluid Circulation Systems. *Geochem. J.* 45, 109–124. doi:10.2343/geochemj.1.0105
- Kawasumi, S., and Chiba, H. (2017). Redox State of Seafloor Hydrothermal Fluids and its Effect on Sulfide Mineralization. *Chem. Geology*. 451, 25–37. doi:10.1016/j.chemgeo.2017.01.001
- Keith, M., Haase, K. M., Häckel, F., Schwarz-Schampera, U., Klemm, R., Hannington, M., et al. (2021). Trace Element Fractionation and Precipitation in Submarine Back-Arc Hydrothermal Systems, Nifonea Caldera, New Hebrides Subduction Zone. *Ore Geology. Rev.* 135, 104211. doi:10.1016/j.oregeorev.2021.104211
- Keith, M., Haase, K. M., Klemm, R., Krumm, S., and Strauss, H. (2016a). Systematic Variations of Trace Element and Sulfur Isotope Compositions in Pyrite with Stratigraphic Depth in the Skouriotissa Volcanic-Hosted Massive Sulfide deposit, Troodos Ophiolite, Cyprus. *Chem. Geology*. 423, 7–18. doi:10.1016/j.chemgeo.2015.12.012
- Keith, M., Häckel, F., Haase, K. M., Schwarz-Schampera, U., and Klemm, R. (2016b). Trace Element Systematics of Pyrite from Submarine Hydrothermal Vents. *Ore Geology. Rev.* 72, 728–745.
- Keith, M., Haase, K. M., Klemm, R., Smith, D. J., Schwarz-Schampera, U., and Bach, W. (2018). Constraints on the Source of Cu in a Submarine Magmatic-Hydrothermal System, Brothers Volcano, Kermadec Island Arc. *Contrib. Mineral. Petrol.* 173, 1–16. doi:10.1007/s00410-018-1470-5
- Keith, M., Haase, K. M., Schwarz-Schampera, U., Klemm, R., Petersen, S., and Bach, W. (2014). Effects of Temperature, Sulfur, and Oxygen Fugacity on the Composition of Sphalerite from Submarine Hydrothermal Vents. *Geology* 42, 699–702. doi:10.1130/g35655.1
- Keith, M., Häckel, F., Haase, K. M., Schwarz-Schampera, U., and Klemm, R. (2016b). Trace Element Systematics of Pyrite from Submarine Hydrothermal Vents. *Ore Geology. Rev.* 72, 728–745. doi:10.1016/j.oregeorev.2015.07.012
- Keith, M., Smith, D. J., Doyle, K., Holwell, D. A., Jenkin, G. R. T., Barry, T. L., et al. (2020). Pyrite Chemistry: A New Window into Au-Te Ore-Forming Processes in Alkaline Epithermal Districts, Cripple Creek, Colorado. *Geochimica et Cosmochimica Acta* 274, 172–191. doi:10.1016/j.gca.2020.01.056
- Kim, J., Son, S.-K., Son, J.-W., Kim, K.-H., Shim, W. J., Kim, C. H., et al. (2009). Venting Sites along the Fonualei and Northeast Lau Spreading Centers and Evidence of Hydrothermal Activity at an off-axis Caldera in the Northeastern Lau Basin. *Geochem. J.* 43, 1–13. doi:10.2343/geochemj.0.0164
- Kleint, C., Bach, W., Diehl, A., Fröhberg, N., Garbe-Schönberg, D., Hartmann, J. F., et al. (2019). Geochemical Characterization of Highly Diverse Hydrothermal Fluids from Volcanic Vent Systems of the Kermadec Intraoceanic Arc. *Chem. Geology*. 528, 119289. doi:10.1016/j.chemgeo.2019.119289
- Koschinsky, A., Garbe-Schönberg, D., Sander, S., Schmidt, K., Gennerich, H.-H., and Strauss, H. (2008). Hydrothermal Venting at Pressure-Temperature Conditions above the Critical point of Seawater, 5°S on the Mid-Atlantic Ridge. *Geol* 36, 615–618. doi:10.1130/g24726a.1
- Labidi, J., Cartigny, P., Birck, J. L., Assayag, N., and Bourrand, J. J. (2012). Determination of Multiple Sulfur Isotopes in Glasses: A Reappraisal of the MORB δ34S. *Chem. Geology*. 334, 189–198. doi:10.1016/j.chemgeo.2012.10.028
- Lupton, J., Rubin, K. H., Arculus, R., Lilley, M., Butterfield, D., Resing, J., et al. (2015). Helium Isotope, C/3He, and Ba-Nb-Ti Signatures in the Northern Lau Basin: Distinguishing Arc, Back-Arc, and Hotspot Affinities. *Geochem. Geophys. Geosyst.* 16, 1133–1155. doi:10.1002/2014gc005625
- Martin, A. J., Keith, M., Parvaz, D. B., McDonald, I., Boyce, A. J., McFall, K. A., et al. (2020). Effects of Magmatic Volatile Influx in Mafic VMS Hydrothermal Systems: Evidence from the Troodos Ophiolite, Cyprus. *Chem. Geology*. 531, 119325. doi:10.1016/j.chemgeo.2019.119325
- Maslennikov, V. V., Maslennikova, S. P., Large, R. R., and Danyushevsky, L. V. (2009). Study of Trace Element Zonation in Vent Chimneys from the Silurian Yaman-Kasy Volcanic-Hosted Massive Sulfide deposit (Southern Urals, Russia) Using Laser Ablation-Inductively Coupled Plasma Mass Spectrometry (LA-ICPMS). *Econ. Geology*. 104, 1111–1141. doi:10.2113/gsecongeo.104.8.1111
- McDermott, J. M., Ono, S., Tivey, M. K., Seewald, J. S., Shanks, W. C., and Solow, A. R. (2015). Identification of Sulfur Sources and Isotopic Equilibria in Submarine Hot-Springs Using Multiple Sulfur Isotopes. *Geochimica et Cosmochimica Acta* 160, 169–187. doi:10.1016/j.gca.2015.02.016
- Meng, X., Li, X., Chu, F., Zhu, J., Lei, J., Li, Z., et al. (2020). Trace Element and Sulfur Isotope Compositions for Pyrite across the Mineralization Zones of a Sulfide Chimney from the East Pacific Rise (1–2°S). *Ore Geology. Rev.* 116, 103209. doi:10.1016/j.oregeorev.2019.103209
- Merle, S., Chadwick, W., and Rubin, K. (2018). Processed Gridded Bathymetry Data from the Tonga Volcanic Arc Acquired during R/V Falkor Expedition FK171110. *Interdiscip. Earth Data Alliance (Ieda0)*. doi:10.1594/IEDA/324447
- Metz, S., and Trefry, J. H. (2000). Chemical and Mineralogical Influences on Concentrations of Trace Metals in Hydrothermal Fluids. *Geochimica et Cosmochimica Acta* 64, 2267–2279. doi:10.1016/s0016-7037(00)00354-9
- Monecke, T., Petersen, S., and Hannington, M. D. (2014). Constraints on Water Depth of Massive Sulfide Formation: Evidence from Modern Seafloor Hydrothermal Systems in Arc-Related Settings. *Econ. Geology*. 109, 2079–2101. doi:10.2113/econgeo.109.8.2079
- Morrison, J., Brockwell, T., Merren, T., Fourle, F., and Phillips, A. M. (2001). On-line High-Precision Stable Hydrogen Isotopic Analyses on Nanoliter Water Samples. *Anal. Chem.* 73, 3570–3575. doi:10.1021/ac001447t
- Mottl, M. J., and Holland, H. D. (1978). Chemical Exchange during Hydrothermal Alteration of basalt by Seawater-I. Experimental Results for Major and Minor Components of Seawater. *Geochimica et Cosmochimica Acta* 42, 1103–1115. doi:10.1016/0016-7037(78)90107-2
- Mottl, M. J., Seewald, J. S., Wheat, C. G., Tivey, M. K., Michael, P. J., Proskurowski, G., et al. (2011). Chemistry of hot springs along the Eastern Lau Spreading Center. *Geochimica et Cosmochimica Acta* 75, 1013–1038. doi:10.1016/j.gca.2010.12.008
- Murowchick, J. B., and Barnes, H. L. (1986). Marcasite Precipitation from Hydrothermal Solutions. *Geochimica et Cosmochimica Acta* 50, 2615–2629. doi:10.1016/0016-7037(86)90214-0
- Naden, J., Kiliass, S. P., and Darbyshire, D. P. F. (2005). Active Geothermal Systems with Entrained Seawater as Modern Analogs for Transitional Volcanic-Hosted Massive Sulfide and continental Magmato-Hydrothermal Mineralization: The Example of Milos Island, Greece. *Geol* 33, 541–544. doi:10.1130/g21307.1
- Nestmeyer, M., Keith, M., Haase, K. M., Klemm, R., Voudouris, P., Schwarz-Schampera, U., et al. (2021). Trace Element Signatures in Pyrite and Marcasite from Shallow Marine Island Arc-Related Hydrothermal Vents, Calypso Vents, New Zealand, and Paleochori Bay, Greece. *Front. Earth Sci.* 9, 1–18. doi:10.3389/feart.2021.641654
- Ono, S., Shanks, W. C., Rouxel, O. J., and Rumble, D. (2007). S-33 Constraints on the Seawater Sulfate Contribution in Modern Seafloor Hydrothermal Vent Sulfides. *Geochimica et Cosmochimica Acta* 71, 1170–1182. doi:10.1016/j.gca.2006.11.017
- Pin, C., and Bassin, C. (1992). Evaluation of a Strontium-specific Extraction Chromatographic Method for Isotopic Analysis in Geological Materials. *Analytica Chim. Acta* 269, 249–255. doi:10.1016/0003-2670(92)85409-y
- Pokrovski, G. S., Borisova, A. Y., and Bychkov, A. Y. (2018). Speciation and Transport of Metals and Metalloids in Geological Vapours. *Thermodyn. Geotherm. Fluids* 76, 165–218.
- Pokrovski, G. S., Roux, J., and Harrichoury, J.-C. (2005). Fluid Density Control on Vapor-Liquid Partitioning of Metals in Hydrothermal Systems. *Geology* 33, 657–660. doi:10.1130/g21475ar.1
- Proskurowski, G., Lilley, M. D., and Olson, E. J. (2008). Stable Isotopic Evidence in Support of Active Microbial Methane Cycling in Low-Temperature Diffuse Flow Vents at 9°50'N East Pacific Rise. *Geochimica et Cosmochimica Acta* 72, 2005–2023. doi:10.1016/j.gca.2008.01.025
- Reed, M. H., and Palandri, J. (2006). 11. Sulfide Mineral Precipitation from Hydrothermal Fluids. *Rev. Mineral. Geochem.* 61, 609–632. doi:10.1515/9781501509490-012
- Reeves, E. P., McDermott, J. M., and Seewald, J. S. (2014). The Origin of Methanethiol in Midocean ridge Hydrothermal Fluids. *Proc. Natl. Acad. Sci.* 111, 5474–5479. doi:10.1073/pnas.1400643111
- Reeves, E. P., Seewald, J. S., Saccoccia, P., Bach, W., Craddock, P. R., Shanks, W. C., et al. (2011). Geochemistry of Hydrothermal Fluids from the PACMANUS, Northeast Pual and Vienna Woods Hydrothermal fields, Manus Basin, Papua New Guinea. *Geochimica et Cosmochimica Acta* 75, 1088–1123. doi:10.1016/j.gca.2010.11.008

- Regelous, M., Collerson, K. D., Ewart, A., and Wendt, J. I. (1997). Trace Element Transport Rates in Subduction Zones: Evidence from Th, Sr and Pb Isotope Data for Tonga-Kermadec Arc Lavas. *Earth Planet. Sci. Lett.* 150, 291–302. doi:10.1016/s0012-821x(97)00107-6
- Resing, J., Embley, R., Baker, E., Baumberger, T., Buck, N., Butterfield, D., et al. (2009). *Northeast Lau Basin Response Cruise (NELRC)*, Thompson Expedition TN-234 1–142.
- Román, N., Reich, M., Leisen, M., Morata, D., Barra, F., and Deditius, A. P. (2019). Geochemical and Micro-textural Fingerprints of Boiling in Pyrite. *Geochimica et Cosmochimica Acta* 246, 60–85. doi:10.1016/j.gca.2018.11.034
- Sakai, H., Marais, D. J. D., Ueda, A., and Moore, J. G. (1984). Concentrations and Isotope Ratios of Carbon, Nitrogen and Sulfur in Ocean-Floor Basalts. *Geochimica et Cosmochimica Acta* 48, 2433–2441. doi:10.1016/0016-7037(84)90295-3
- Schaarschmidt, A., Haase, K. M., Klemm, R., Keith, M., Voudouris, P. C., Alferis, D., et al. (2021). Boiling Effects on Trace Element and Sulfur Isotope Compositions of Sulfides in Shallow-marine Hydrothermal Systems: Evidence from Milos Island, Greece. *Chem. Geology*. 583, 120457. doi:10.1016/j.chemgeo.2021.120457
- Schmidt, K., Garbe-Schönberg, D., Hannington, M. D., Anderson, M. O., Bühring, B., Haase, K., et al. (2017). Boiling Vapour-type Fluids from the Nifonea Vent Field (New Hebrides Back-Arc, Vanuatu, SW Pacific): Geochemistry of an Early-Stage, post-eruptive Hydrothermal System. *Geochimica et Cosmochimica Acta* 207, 185–209. doi:10.1016/j.gca.2017.03.016
- Schmidt, K., Garbe-Schönberg, D., Bau, M., and Koschinsky, A. (2010). Rare Earth Element Distribution in >400°C Hot Hydrothermal Fluids from 5°S, MAR: The Role of Anhydrite in Controlling Highly Variable Distribution Patterns. *Geochim. Cosmochim. Acta*. 4058, 728–4077. doi:10.1016/j.gca.2010.04.007
- Seewald, J. S., Reeves, E. P., Bach, W., Saccocia, P. J., Craddock, P. R., Shanks, W. C., et al. (2015). Submarine Venting of Magmatic Volatiles in the Eastern Manus Basin, Papua New Guinea. *Geochimica et Cosmochimica Acta* 163, 178–199. doi:10.1016/j.gca.2015.04.023
- Seewald, J. S., Reeves, E. P., Bach, W., Saccocia, P. J., Craddock, P. R., Walsh, E., et al. (2019). Geochemistry of Hot-Springs at the SuSu Knolls Hydrothermal Field, Eastern Manus Basin: Advanced Argillic Alteration and Vent Fluid Acidity. *Geochimica et Cosmochimica Acta* 255, 25–48. doi:10.1016/j.gca.2019.03.034
- Seewald, J. S., Seyfried, W. E., and Shanks, W. C. (1994). Variations in the Chemical and Stable Isotope Composition of Carbon and Sulfur Species during Organic-Rich Sediment Alteration: An Experimental and Theoretical Study of Hydrothermal Activity at Guaymas basin, Gulf of California. *Geochimica et Cosmochimica Acta* 58, 5065–5082. doi:10.1016/0016-7037(94)90232-1
- Seewald, J. S., and Seyfried, W. E. (1990). The Effect of Temperature on Metal Mobility in Subseafloor Hydrothermal Systems: Constraints from basalt Alteration Experiments. *Earth Planet. Sci. Lett.* 101, 388–403. doi:10.1016/0012-821x(90)90168-w
- Seyfried, W. E., and Ding, K. (1995). Phase Equilibria in Subseafloor Hydrothermal Systems: A Review of the Role of Redox, Temperature, pH and Dissolved Cl on the Chemistry of Hot spring Fluids at Mid-ocean Ridges. *Geophys. Monogr. Ser.* 91, 248–272.
- Seyfried, W. E., Janecky, D. R., and Mottl, M. J. (1984). Alteration of the Oceanic Crust: Implications for Geochemical Cycles of Lithium and boron. *Geochimica et Cosmochimica Acta* 48, 557–569. doi:10.1016/0016-7037(84)90284-9
- Seyfried, W. E., and Mottl, M. J. (1982). Hydrothermal Alteration of basalt by Seawater under Seawater-Dominated Conditions. *Geochimica et Cosmochimica Acta* 46, 985–1002. doi:10.1016/0016-7037(82)90054-0
- Seyfried, W. E., Seewald, J. S., Berndt, M. E., Ding, K., and Foustoukos, D. I. (2003). Chemistry of hydrothermal vent fluids from the Main Endeavour Field, northern Juan de Fuca Ridge: Geochemical controls in the aftermath of June 1999 seismic events. *J. Geophys. Res.* 108, 1–23. doi:10.1029/2002jb001957
- Shanks, W. C., Böhlke, J. K., and Seal, R. R. (1995). Stable Isotopes in Mid-ocean ridge Hydrothermal Systems: Interactions between Fluids, Minerals, and Organisms. *Geophys. Monogr. Ser.* 91, 194–221. doi:10.1029/GM091p0194
- Shanks, W. C. (2001). Stable Isotopes in Seafloor Hydrothermal Systems: Vent Fluids, Hydrothermal Deposits, Hydrothermal Alteration, and Microbial Processes. *Rev. Mineralogy Geochem.* 43, 469–525. doi:10.2138/gsrmg.43.1.469
- Stoffers, P., Worthington, T. J., Schwarz-Schampera, U., Hannington, M. D., Massoth, G. J., Hekinian, R., et al. (2006). Submarine Volcanoes and High-Temperature Hydrothermal Venting on the Tonga Arc, Southwest Pacific. *Geol* 34, 453–456. doi:10.1130/g22227.1
- Storch, B., Haase, K. M., Romer, R. H. W., Beier, C., and Koppers, A. A. P. (2020). Rifting of the Oceanic Azores Plateau with Episodic Volcanic Activity. *Sci. Rep.* 10, 1–12. doi:10.1038/s41598-020-76691-1
- Stucker, V. K., Walker, S. L., de Ronde, C. E. J., Caratori Tontini, F., and Tsuchida, S. (2017). Hydrothermal Venting at Hinepua Submarine Volcano, Kermadec Arc: Understanding Magmatic-Hydrothermal Fluid Chemistry. *Geochem. Geophys. Geosyst.* 18, 3646–3661. doi:10.1002/2016gc006713
- Tardani, D., Reich, M., Deditius, A. P., Chrysosoulis, S., Sánchez-Alfaro, P., Wrage, J., et al. (2017). Copper-arsenic Decoupling in an Active Geothermal System: A Link between Pyrite and Fluid Composition. *Geochimica et Cosmochimica Acta* 204, 179–204. doi:10.1016/j.gca.2017.01.044
- Tassi, F., Vaselli, O., Papazachos, C. B., Giannini, L., Chiodini, G., Vougioukalakis, G. E., et al. (2013). Geochemical and Isotopic Changes in the Fumarolic and Submerged Gas Discharges during the 2011–2012 Unrest at Santorini Caldera (Greece). *Bull. Volcanol.* 75, 1–15. doi:10.1007/s00445-013-0711-8
- Tivey, M. K., Stakes, D. S., Cook, T. L., Hannington, M. D., and Petersen, S. (1999). A model for growth of steep-sided vent structures on the Endeavour Segment of the Juan de Fuca Ridge: Results of a petrologic and geochemical study. *J. Geophys. Res.* 104, 22859–22883. doi:10.1029/1999jb900107
- Tivey, M. K. (1995). The Influence of Hydrothermal Fluid Composition and Advection Rates on Black Smoker Chimney Mineralogy: Insights from Modeling Transport and Reaction. *Geochimica et Cosmochimica Acta* 59, 1933–1949. doi:10.1016/0016-7037(95)00118-2
- Tostevin, R., Turchyn, A. V., Farquhar, J., Johnston, D. T., Eldridge, D. L., Bishop, J. K. B., et al. (2014). Multiple Sulfur Isotope Constraints on the Modern Sulfur Cycle. *Earth Planet. Sci. Lett.* 396, 14–21. doi:10.1016/j.epsl.2014.03.057
- van Acherbergh, E., Ryan, C. G., and Griffin, W. L. (2000). *GLITTER: On-Line Interactive Data Reduction for LA-ICP-MS*. Sydney, Australia: Macquarie Research Ltd.
- Van Geldern, R., and Barth, J. A. C. (2012). Optimization of Instrument Setup and post-run Corrections for Oxygen and Hydrogen Stable Isotope Measurements of Water by Isotope Ratio Infrared Spectroscopy (IRIS). *Limnol. Oceanogr. Methods* 10, 1024–1036. doi:10.4319/lom.2012.10.1024
- Verati, C., Lancelot, J., and Hékinian, R. (1999). Pb Isotope Study of Black-Smokers and Basalts from Pito Seamount Site (Easter Microplate). *Chem. Geology*. 155, 45–63. doi:10.1016/s0009-2541(98)00140-5
- Von Damm, K. L., Buttermore, L. G., Oosting, S. E., Bray, A. M., Fornari, D. J., Lilley, M. D., et al. (1997). Direct Observation of the Evolution of a Seafloor 'black Smoker' from Vapor to Brine. *Earth Planet. Sci. Lett.* 149, 101–111. doi:10.1016/s0012-821x(97)00059-9
- Von Damm, K. L. (1995). Controls on the Chemistry and Temporal Variability of Seafloor Hydrothermal Fluids. *Geophys. Monogr. Ser.* 91, 222–247. doi:10.1029/GM091p0222
- Von Damm, K. L., Edmond, J. M., Grant, B., Measures, C. I., Walden, B., and Weiss, R. F. (1985a). Chemistry of Submarine Hydrothermal Solutions at 21 °N, East Pacific Rise. *Geochimica et Cosmochimica Acta* 49, 2197–2220. doi:10.1016/0016-7037(85)90222-4
- Von Damm, K. L., Edmond, J. M., Measures, C. I., and Grant, B. (1985b). Chemistry of Submarine Hydrothermal Solutions at Guaymas Basin, Gulf of California. *Geochimica et Cosmochimica Acta* 49, 2221–2237. doi:10.1016/0016-7037(85)90223-6
- Voudouris, P., Kati, M., Magganas, A., Keith, M., Valsami-Jones, E., Haase, K. M., et al. (2021). Arsenian Pyrite and Cinnabar from Active Submarine Nearshore Vents, Paleochori Bay, Milos Island, Greece. *Minerals* 11, 1–25.
- Wang, B.-S., You, C.-F., Huang, K.-F., Wu, S.-F., Aggarwal, S. K., Chung, C.-H., et al. (2010). Direct Separation of boron from Na- and Ca-Rich Matrices by Sublimation for Stable Isotope Measurement by MC-ICP-MS. *Talanta* 82, 1378–1384. doi:10.1016/j.talanta.2010.07.010
- Webber, A. P., Roberts, S., Murton, B. J., and Hodgkinson, M. R. S. (2015). Geology, Sulfide Geochemistry and Supercritical Venting at the Beebe Hydrothermal Vent Field, Cayman Trough. *Geochem. Geophys. Geosyst.* 16, 2661–2678. doi:10.1002/2015gc005879

- Welhan, J. A. (1988). Origins of Methane in Hydrothermal Systems. *Chem. Geology*. 71, 183–198. doi:10.1016/0009-2541(88)90114-3
- Wendt, J. I., Regelous, M., Collerson, K. D., and Ewart, A. (1997). Evidence for a Contribution from Two Mantle Plumes to Island-Arc Lavas from Northern Tonga. *Geol* 25, 611–614. doi:10.1130/0091-7613(1997)025<0611:efact>2.3.co;2
- Wilckens, F. K., Reeves, E. P., Bach, W., Meixner, A., Seewald, J. S., Koschinsky, A., et al. (2018). The Influence of Magmatic Fluids and Phase Separation on B Systematics in Submarine Hydrothermal Vent Fluids from Back-Arc Basins. *Geochimica et Cosmochimica Acta* 232, 140–162. doi:10.1016/j.gca.2018.04.023
- Wohlgemuth-Ueberwasser, C. C., Viljoen, F., Petersen, S., and Vorster, C. (2015). Distribution and Solubility Limits of Trace Elements in Hydrothermal Black Smoker Sulfides: An *In-Situ* LA-ICP-MS Study. *Geochimica et Cosmochimica Acta* 159, 16–41. doi:10.1016/j.gca.2015.03.020
- Yamaoka, K., Hong, E., Ishikawa, T., Gamo, T., and Kawahata, H. (2015). Boron Isotope Geochemistry of Vent Fluids from Arc/back-Arc Seafloor Hydrothermal Systems in the Western Pacific. *Chem. Geology*. 392, 9–18. doi:10.1016/j.chemgeo.2014.11.009
- Zellmer, K. E., and Taylor, B. (2001). A Three-Plate Kinematic Model for Lau Basin Opening. *Geochem. Geophys. Geosystems* 2, 1–26. doi:10.1029/2000gc000106
- Zeng, Z., Ma, Y., Chen, S., Selby, D., Wang, X., and Yin, X. (2017). Sulfur and lead Isotopic Compositions of Massive Sulfides from Deep-Sea Hydrothermal Systems: Implications for Ore Genesis and Fluid Circulation. *Ore Geology. Rev.* 87, 155–171. doi:10.1016/j.oregeorev.2016.10.014
- Zhang, H., Yan, Q., Li, C., Zhu, Z., Zhao, R., and Shi, X. (2019a). Geochemistry of Diverse Lava Types from the Lau Basin (South West Pacific): Implications for Complex Back-arc Mantle Dynamics. *Geol. J.* 54, 3643–3659. doi:10.1002/gj.3354
- Zhang, X., Zhai, S., Yu, Z., Yang, Z., and Xu, J. (2019b). Zinc and lead Isotope Variation in Hydrothermal Deposits from the Okinawa Trough. *Ore Geology. Rev.* 111, 102944. doi:10.1016/j.oregeorev.2019.102944

Conflict of Interest: The authors declare that the research was conducted in the absence of any commercial or financial relationships that could be construed as a potential conflict of interest.

Publisher's Note: All claims expressed in this article are solely those of the authors and do not necessarily represent those of their affiliated organizations, or those of the publisher, the editors, and the reviewers. Any product that may be evaluated in this article, or claim that may be made by its manufacturer, is not guaranteed or endorsed by the publisher.

Copyright © 2021 Klose, Keith, Hafermaas, Kleint, Bach, Diehl, Wilckens, Peters, Strauss, Klemm, van Geldern, Haase and Koschinsky. This is an open-access article distributed under the terms of the Creative Commons Attribution License (CC BY). The use, distribution or reproduction in other forums is permitted, provided the original author(s) and the copyright owner(s) are credited and that the original publication in this journal is cited, in accordance with accepted academic practice. No use, distribution or reproduction is permitted which does not comply with these terms.